IMAGING

The PET tracer [^{11}C]MODAG-005 targets alpha-synuclein aggregates in the brain

Ran Sing Saw[1]†, Sabrina Haas[1]†, Felix Schmidt[2]†, Sergey Ryazanov[2,3]†, Andrei Leonov[2,3]†, Daniel Bleher[1], Ann-Kathrin Grotegerd[1], Laura Kuebler[1], Benjamin Roeben[4,5,6], Fabian Schmidt[1,7], Matthias Reimold[7], Federica Bonanno[1], Viktoria C. Ruf[8], Bernadette Dahl[5,6,9], Christine M. Sandiego[10], Kelly E. Henry[10], Ioannis Papadopoulos[1], Martin Schaller[11], Philipp J. Kahle[5,6], Johannes Levin[2,12,13,14], Thomas Gasser[4,5], Kathrin Brockmann[4,5,6], Gerald Reischl[1,15], Christian la Fougère[7,15], Bernd J. Pichler[1,15], Andreas Maurer[1,15], Christian Griesinger[3,16]*, Armin Giese[2]*, Kristina Herfert[1]*

Synucleinopathies are neurodegenerative diseases characterized by the presence of brain inclusions containing the pathologically aggregated protein α-synuclein. The development of a positron emission tomography tracer to detect aggregates of misfolded α-synuclein could revolutionize early diagnosis, disease monitoring, and the evaluation of therapeutic efficacy. Here, we present the development, preclinical validation, and first-in-human evaluation of [^{11}C]MODAG-005. In vitro binding experiments demonstrated subnanomolar binding affinity to recombinant α-synuclein fibrils and to α-synuclein inclusions in human brain tissue. Specific binding in multiple system atrophy (MSA) brain tissue was detected using autoradiography and microautoradiography and was validated through immunostaining. In vivo, [^{11}C]MODAG-005 showed good brain penetration, rapid clearance from brain tissue, and low metabolite formation in rodents and nonhuman primates. In addition, a pronounced binding and a good signal-to-noise ratio were achieved in an α-synuclein fibril–injected rat model and in an α-synuclein (A30P) transgenic mouse model in correlation to the pathological load. To validate the potential of [^{11}C]MODAG-005 for therapeutic development, we showed target engagement of the drug candidate anle138b in the brain tissues from α-synuclein (A30P) mice and patients with multiple system atrophy as well as in vivo in α-synuclein fibril–injected rats. Last, first-in-human imaging demonstrated [^{11}C]MODAG-005 binding in brain regions affected by α-synuclein pathology in patients with clinically established MSA cerebellar type, MSA cerebellar and parkinsonian type, and Parkinson's disease.

INTRODUCTION

Synucleinopathies, such as Parkinson's disease (PD), dementia with Lewy bodies, and multiple system atrophy (MSA), are neurodegenerative diseases that pose a substantial threat to our aging society. A definitive diagnosis is now only possible by postmortem autopsy (*1*). Their shared neuropathological hallmark is the presence of misfolded α-synuclein (α-Syn), which appears with a spatial distribution in the brain that depends on the stage and type of disease. The accumulation of pathological α-Syn begins years before the onset of the first (motor) symptoms and would therefore be an excellent biomarker for early detection and monitoring of disease progression (*2*).

Positron emission tomography (PET) is a noninvasive imaging technology that traces a radioactively labeled molecule designed for a certain biological target in vivo (*3*). In Alzheimer's disease (AD), the development of PET tracers targeting amyloid-β (Aβ) and tau aggregates has greatly advanced our understanding of the time course of aggregation and the regional spread of pathology, revolutionizing the early diagnosis of AD and the assessment of therapeutic effects. Several small molecules targeting α-Syn aggregates have been developed over the past decade, with a few of them being studied in human participants (*4*–*9*). Nonetheless, none of these molecules has been translated into clinical applications so far. Compared with Aβ and tau, researchers have encountered considerable challenges in their search for an α-Syn PET tracer, mainly because of the low availability of the target, which requires a highly specific molecule with little to no background binding. In addition, misfolded α-Syn contains β-sheet secondary structural elements that resemble those of other misfolded peptides and proteins, such as Aβ or tau, which are also found as copathologies. Fibril polymorphism is another challenge that further complicates the development of a specific and selective radiotracer because of the multiple conformations of α-Syn fibrils (*10*, *11*). Because α-Syn aggregates are located intracellularly, a molecule that penetrates both the blood-brain barrier

[1]Werner Siemens Imaging Center, Department of Preclinical Imaging and Radiopharmacy, University of Tuebingen, 72076 Tuebingen, Germany. [2]MODAG GmbH, 55234 Wendelsheim, Germany. [3]Department of NMR-based Structural Biology, Max Planck Institute for Multidisciplinary Sciences, 37077 Goettingen, Germany. [4]Department of Neurology, Eberhard Karls University Tuebingen, 72076 Tuebingen, Germany. [5]Hertie Institute for Clinical Brain Research, Department of Neurodegenerative Diseases, Eberhard Karls University Tuebingen, 72076 Tuebingen, Germany. [6]German Center for Neurodegenerative Diseases, 72076 Tuebingen, Germany. [7]Nuclear Medicine and Clinical Molecular Imaging, Department of Radiology, University Hospital Tuebingen, 72076 Tuebingen, Germany. [8]Ludwig Maximilians University, Center for Neuropathology and Prion Research, 81377 Munich, Germany. [9]Graduate School of Cellular and Molecular Neuroscience, Eberhard Karls University Tuebingen, 72076 Tuebingen, Germany. [10]Invicro LLC, Needham, MA 02494, USA. [11]Department of Dermatology, Eberhard Karls University Tuebingen, 72076 Tuebingen, Germany. [12]Department of Neurology, Ludwig-Maximilians-University Munich, Munich, Germany. [13]German Center for Neurodegenerative Diseases (DZNE), site Munich, Munich, Germany. [14]Munich Cluster for Systems Neurology (SyNergy), Munich, Germany. [15]Cluster of Excellence iFIT (EXC 2180) "Image-Guided and Functionally Instructed Tumor Therapies", Eberhard Karls University Tuebingen, 72076 Tuebingen, Germany. [16]Cluster of Excellence "Multiscale Bioimaging: From Molecular Machines to Networks of Excitable Cells" (MBExC), University of Goettingen; 37075 Goettingen, Germany.
†These authors contributed equally to this work.
*Corresponding author. Email: kristina.herfert@med.uni-tuebingen.de (K.H.); giese@modag.net (A.G.); cigr@mpinat.mpg.de (C.G.)

and the cell membrane is required. Furthermore, the highly complex structure of Lewy bodies, consisting of lipophilic organelles and membrane fragments, presents an additional barrier to α-Syn fibril binding (*12*).

We previously developed two radiolabeled α-Syn–targeting tracers that are structurally derived from the lead compound anle138b (emrusolmin) (*13*): anle253b and its successor MODAG-001 (*14*, *15*). MODAG-001 exhibited high affinity for recombinant α-Syn fibrils and a favorable in vivo pharmacokinetic profile, and it was able to detect injected recombinant α-Syn fibrils in rats (*14*). In pigs, (d_3)-[^{11}C]MODAG-001 had excellent brain kinetics and a confirmed specific binding in an α-Syn pig model in vivo (*16*). However, in human brain tissue, no to only very low binding could be observed because of its high nonspecific binding, lowering the signal-to-noise ratio (SNR) in the target tissue. Nonetheless, its high affinity and promising pharmacokinetic properties formed the basis for the development and testing of next-generation compounds with reduced nonspecific binding. Here, we report the development, preclinical evaluation, and first-in-human study of an α-Syn PET tracer candidate, [^{11}C]MODAG-005, the demethylated form of [^{11}C]MODAG-001.

RESULTS

[^{3}H]MODAG-005 shows binding specificity for recombinant human α-Syn fibrils in cell-free assays

A competition binding assay using [^{3}H]MODAG-001 as the reference compound was performed to evaluate the binding affinity of MODAG-005 toward α-Syn fibrils and revealed a high binding affinity [inhibition constant (K_i) = 0.4 nM] for MODAG-005 (Fig. 1A).

In vitro binding affinity of [^{3}H]MODAG-005 to α-Syn fibrils and selectivity over tau and A$\beta_{1\text{-}42}$ fibrils were determined using saturation binding assays ($n = 3$). Binding specificity and selectivity, which is shown in the binding potential [BP = B_{max}/dissociation constant (K_d), where B_{max} refers to the number of binding sites], was highest toward α-Syn fibrils (BP = 33), which is 200-fold higher compared with tau (BP = 0.17) and 6300-fold higher compared with A$\beta_{1\text{-}42}$ fibrils (BP = 0.0052) (Fig. 1B). [^{3}H]MODAG-005 showed a very high affinity toward α-Syn fibrils ($K_d = 0.2 \pm 0.03$ nM) with low nonspecific binding (Fig. 1C). A 36-fold and >100-fold lower affinity was observed toward tau ($K_d = 7.1 \pm 0.7$ nM) and A$\beta_{1\text{-}42}$ ($K_d = 21 \pm 7.7$ nM) fibrils, respectively (Fig. 1, D and E). MODAG-005 was further tested for off-target binding in a Cerep panel, and no relevant off-target binding was identified. Specific focus was put on monoamine oxidase B (MAO-B) because this was reported to be overexpressed in several proteinopathies (*17*). The median inhibitory concentration (IC_{50}) value for MAO-B was 0.8 μM.

[^{3}H]MODAG-005 binds specifically to α-Syn pathology in human and mouse brain tissue

Figure 2 and fig. S1 show [^{3}H]MODAG-005 autoradiography and α-Syn pSer^{129} immunofluorescence microscopy images of the cerebellar cortex tissue from two donors with MSA and two control donors (see table S1 for an overview of the human tissues used). In macroscopic autoradiography, MSA tissue showed specific binding of [^{3}H]MODAG-005 in the white matter of the cerebellum and

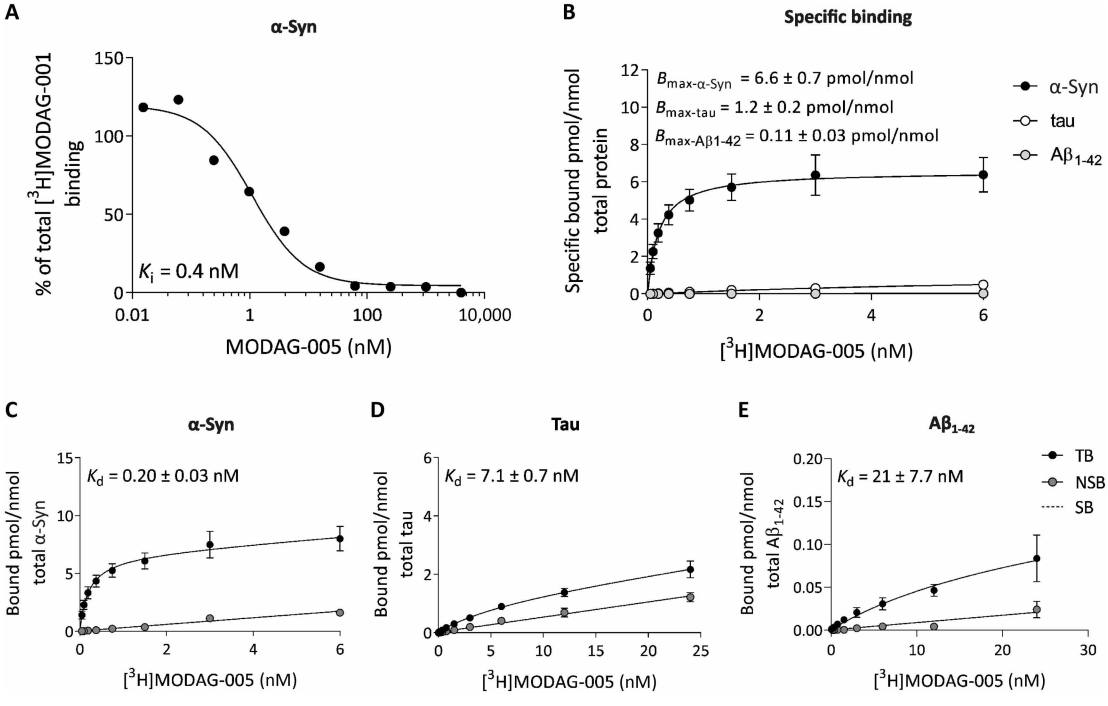

Fig. 1. [^{3}H]MODAG-005 shows high in vitro binding specificity for recombinant human α-Syn fibrils compared with tau and synthetic human A$\beta_{1\text{-}42}$ fibrils. (**A**) Cell-free competition binding experiment ($n = 1$, no replicates). α-Syn fibrils were incubated with 1 nM [^{3}H]MODAG-001, and displacement was induced by different concentrations of unlabeled MODAG-005. (**B**) Saturation binding experiments ($N = 3$ independent experiments) were performed in triplicates showing the binding affinities of [^{3}H]MODAG-005 for α-Syn, tau, and A$\beta_{1\text{-}42}$ fibrils (performed on the same fibril batch, $n = 1$ biological replicate). Nonlinear regression of TB and NSB for (**C**) α-Syn, (**D**) tau, and (**E**) A$\beta_{1\text{-}42}$ fibrils. Data in (B) to (E) are the means ± SD. NSB, nonspecific binding; SB, specific binding; TB, total binding.

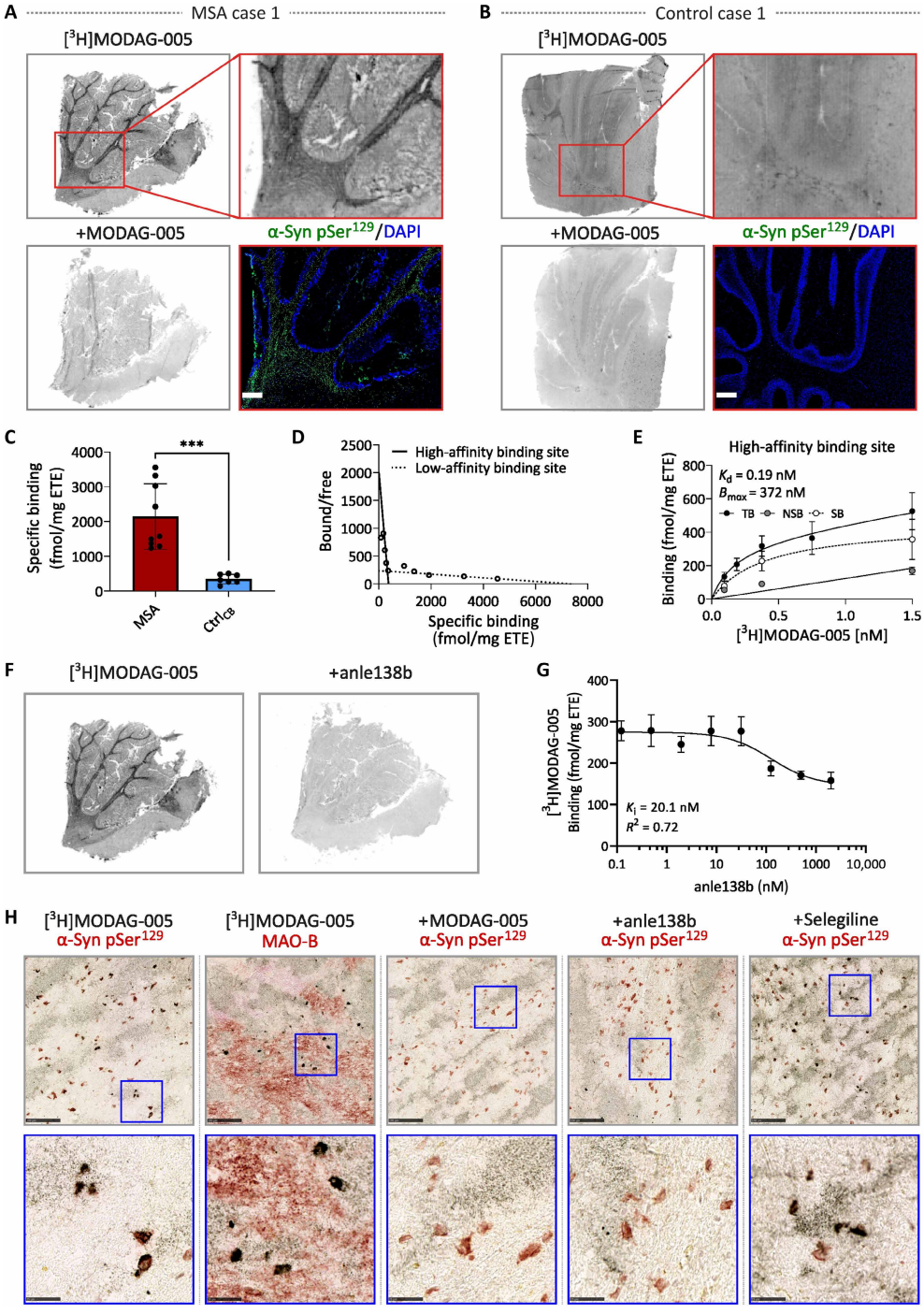

Fig. 2. [^{3}H]MODAG-005 binds to α-Syn pathology and demonstrates target engagement of anle138b in postmortem human MSA brain tissues. (**A** and **B**) Macroscopic autoradiographs showing binding of [^{3}H]MODAG-005 to MSA white matter with verified α-Syn pathology (A) and control tissue with the absence of pathology (B). Pathology in tissue was verified by immunofluorescence of α-Syn pSer^{129} (green) and DAPI (blue). Scale bars, 1 mm. All tissue sections were incubated in the presence of 3 nM [^{3}H]MODAG-005 and 3 μM MODAG-005 for blocking. (**C**) Quantitative analysis of autoradiography [$P = 0.0003$, $n = 2$ biological replicates, $N = 1$ independent experiment with different regions of interest (ROIs) in the same sample; two-way unpaired *t* test with Welch's correction]. (**D**) Scatchard plot based on calculated specific binding revealing two binding sites in MSA tissue. (**E**) Saturation binding curve showing the high-affinity binding site in MSA tissue ($n = 1$ biological replicate, $N = 1$ independent experiment for each tracer concentration with different ROIs in the same sample). (**F**) Macroscopic autoradiography illustrating successful blocking of [^{3}H]MODAG-005 by anle138b in MSA white matter. Tissue sections were incubated in the presence of 3 nM [^{3}H]MODAG-005 and 3 μM anle138b for blocking. (**G**) Competition binding with anle138b in MSA tissue ($n = 1$ biological replicate, $N = 1$ independent experiment for each tracer concentration with different ROIs in the same sample). (**H**) Microautoradiography (60 nM [^{3}H]MODAG-005, silver grains) with immunohistochemistry of α-Syn pSer^{129} or MAO-B (red) showing the specificity of tracer binding to α-Syn pathology. Scale bars, 100 μm (gray boxes) and 25 μm (blue boxes). Data in (C), (E), and (G) are the means ± SD. DAPI, 4′,6-diamidino-2-phenylindole; ETE, estimated tissue equivalent; R^2, coefficient of determination.

cerebellar nuclei, which was blocked by an excess of unlabeled MODAG-005 (Fig. 2A and fig. S1A). α-Syn pathology in the white matter was confirmed by α-Syn pSer^{129} immunofluorescence microscopy. No specific binding and immunofluorescent signal were observed in the control case (Fig. 2B and fig. S1B). [^{3}H]MODAG-005 binding to α-Syn pathology was confirmed by α-Syn pSer^{129} immunofluorescence microscopy. Quantitative analysis showed increased specific binding in the cerebellar white matter of donors with MSA compared with that in control donors ($P = 0.003$) (Fig. 2C).

In saturation binding autoradiography on MSA brain tissue, the Scatchard plot revealed one high- and one low-affinity binding site of [^{3}H]MODAG-005 (Fig. 2D). A K_d of 0.19 nM was determined for the high-affinity binding site (Fig. 2E), which is consistent with K_d values determined on recombinant human fibrils (Fig. 1C). The high-affinity binding site of [^{3}H]MODAG-005 remained after preblocking with the monoamine oxidase B (MAO-B) inhibitor selegiline (fig. S1, C and D). To confirm the absence of copathology in both MSA cases, pTau and Aβ staining was performed in addition to α-Syn pSer^{129} (fig. S2).

Furthermore, target engagement of the potential therapeutic compound anle138b was examined on human MSA brain tissues (Fig. 2, F to H). In macroscopic autoradiography, anle138b was able to block [^{3}H]MODAG-005 binding to α-Syn pathology in the white matter of MSA tissue (Fig. 2F) with a K_i value of 20.1 nM as revealed by a competition experiment (Fig. 2G).

Binding specificity of [^{3}H]MODAG-005 was also demonstrated by microautoradiography showing the colocalization of [^{3}H]MODAG-005 signals with α-Syn aggregates and successful blocking by unlabeled MODAG-005 and anle138b (Fig. 2H). Furthermore, both the lack of colocalization between silver grains and MAO-B staining and the inability of selegiline to block tracer signal indicated that the detected microautoradiography signal of [^{3}H]MODAG-005 in MSA tissue was mainly specific to α-Syn and not due to MAO-B binding (Fig. 2H). Microautoradiography was further performed on substantia nigra (SN) and locus coeruleus tissue from a donor with PD, showing preliminary evidence of target engagement (fig. S3).

[^{3}H]MODAG-005 binding in the frontal cortices of one patient with PD, one patient with AD, and one patient with progressive supranuclear palsy (PSP) was increased compared with that in the control individual (fig. S4, A and B). To examine the binding of [^{3}H]MODAG-005 to α-Syn aggregates in PD tissue, correlation analysis of autoradiography binding and α-Syn pSer^{129} immunofluorescence microscopy indicated a moderate and significant correlation between the two signals ($P < 0.0001$) (fig. S4C). Off-target binding in AD brain tissue slices revealed two binding sites with K_d values of 1.6 and >500 nM (fig. S5). Pathologies in the brain tissues were validated using immunofluorescence staining of α-Syn pSer^{129}, pTau, and Aβ, as shown in fig. S6 and table S1.

In addition, the binding of [^{3}H]MODAG-005 and target engagement of anle138b were confirmed on brain tissue sections of the α-Syn(A30P) mouse model of PD and age-matched wild-type mice (fig. S7A). Quantitative analysis in brain regions with positive α-Syn pSer^{129} immunofluorescence signals revealed more pronounced binding in the midbrains, brainstems, zonae incertae, and cerebella of α-Syn(A30P) compared with those of the wild-type mice (figs. S7B and S8). In the cortex, no differences were observed. The promising in vitro target binding profile led us to label MODAG-005 with carbon-11 to study its in vivo pharmacokinetics and radiometabolite formation.

Pharmacokinetic and metabolic profiles in rodents demonstrate the potential of [^{3}H]MODAG-005 for in vivo brain imaging

After successful synthesis of [^{11}C]MODAG-005 (Fig. 3A), dynamic PET scans were performed in mice and rats. Figure 3B shows whole-body sagittal [^{11}C]MODAG-005 PET/magnetic resonance imaging (MRI) images from one exemplary mouse over time. Time-activity curves (TACs) of selected brain regions and peripheral organs revealed rapid brain uptake, with a peak standardized uptake value (SUV) of 1.9, and a fast washout from the brain, with clearance half-lives ranging from 5.5 to 6.7 min in the selected brain regions (Fig. 3C). TACs of selected brain regions from one rat after injection of [^{11}C]MODAG-005 revealed SUVs up to 3.2 (fig. S9A) and a fast washout from the brain, with clearance half-lives ranging from 3.1 to 6.1 min. [^{11}C]MODAG-005 radio-metabolite formation in the brains and plasma of mice (Fig. 3D) was determined at 5 and 15 min after tracer injection. Quantitative analysis revealed one metabolite in the brain and showed that 96 ± 1.1% and 79 ± 3.1% of the parent compound remained at 5 and 15 min after tracer injection, respectively. Similar results were found in a rat (fig. S9B). Table S2 summarizes quantitative values of all radio-metabolites obtained in plasma and brain.

[^{3}H]MODAG-005 binds specifically to injected α-Syn fibrils in vivo in rats

To investigate whether we can detect [^{11}C]MODAG-005 binding to α-Syn fibrils in vivo, rats were injected with α-Syn fibrils into the right striatum; sham injection with buffer was performed on the contralateral side. Four days postinjection, [^{11}C]MODAG-005 PET images were acquired, and brains were surgically extracted to confirm α-Syn fibril location using thioflavin S (ThS) staining and [^{3}H]MODAG-005 autoradiography. In addition, [^{11}C]MODAG-005 PET images were acquired from noninjected wild-type animals to exclude the possible contribution of blood-brain barrier leakage to increased tracer uptake because of intracranial injections. Figure 4A shows exemplary [^{11}C]MODAG-005 PET images of one α-Syn fibril–injected rat and one noninjected rat summed up from 2.5 to 60 min. Increased tracer accumulation was seen at the α-Syn fibril injection site, colocalizing with in vitro ThS staining and [^{3}H]MODAG-005 autoradiography. Elevated tracer retention in the fibril-injected striatum compared with the sham-injected striatum was detected in time-SUV and time–standardized uptake value ratio (SUVR) curves and in average SUVR calculated using the cerebellum as the reference region (Fig. 4B and fig. S10A). Average SUVR showed increased tracer binding in the fibril-injected compared with the sham-injected striata of α-Syn fibril–injected rats ($P = 0.0003$) but no difference between the right and left striata of noninjected rats ($P = 0.54$) (Fig. 4C). Furthermore, fig. S11 shows the improved SNR by direct comparison of d_3-[^{11}C]MODAG-001 and [^{11}C]MODAG-005 PET images of α-Syn fibril–injected rats at 4 days postinjection.

To investigate and exclude that the elevated tracer binding was due to an inflammatory process or possible MAO-B binding, we performed immunohistochemistry of glial fibrillary acidic protein (GFAP) as a surrogate marker of astrogliosis and MAO-B. Stronger, diffuse staining was observed in the fibril-injected striata compared with the sham-injected striata for both markers. The strongest astrogliosis and MAO-B expression was found in the cortex in both brain hemispheres (fig. S10B), differing from the pattern of in vivo [^{11}C]MODAG-005 PET signal (Fig. 4A).

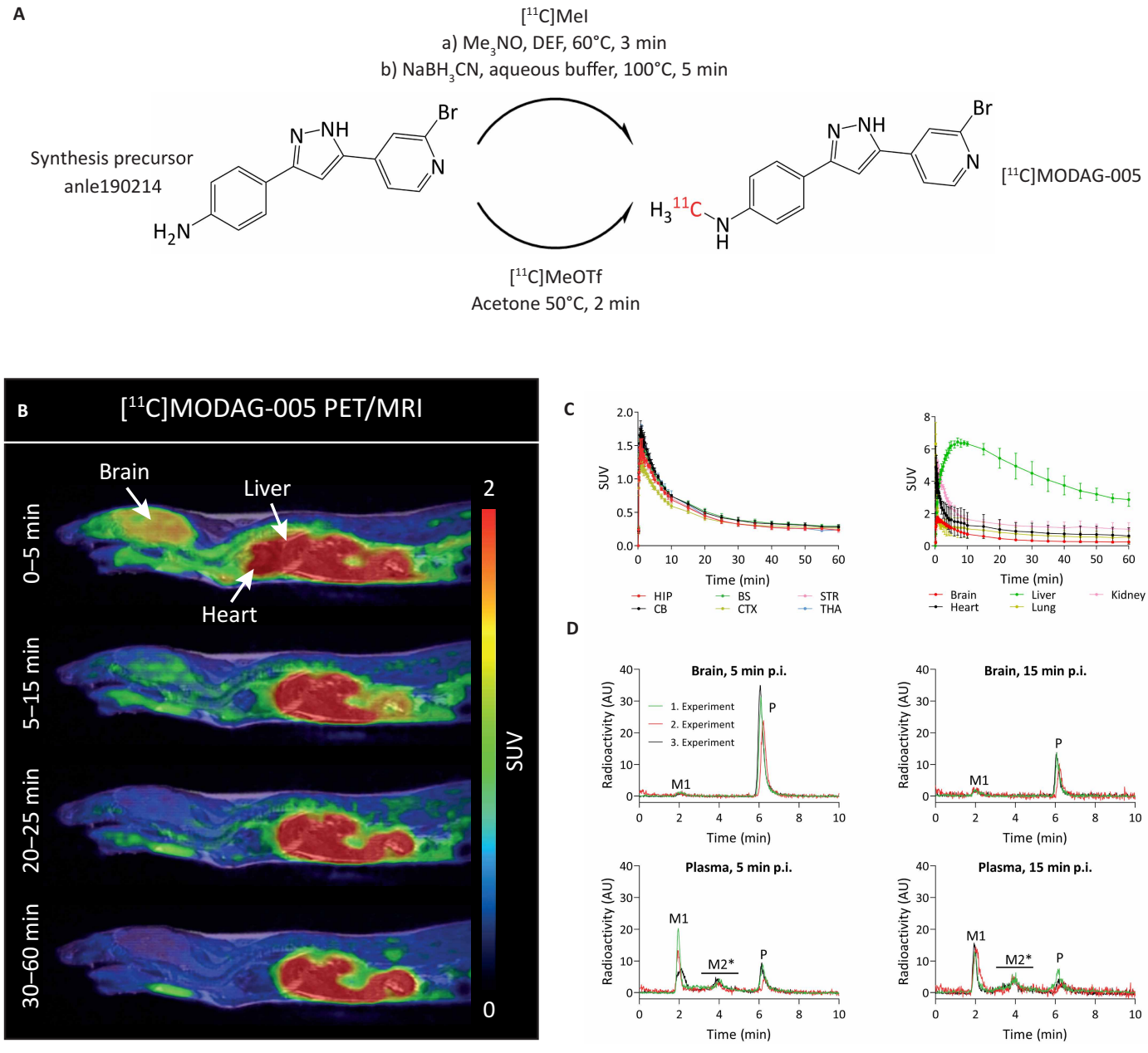

Fig. 3. Radiolabeling and in vivo characterization of [^{11}C]MODAG-005 in healthy mice. (**A**) Illustration of [^{11}C]MODAG-005 radiolabeling by reductive methylation or direct methylation. (**B**) Representative whole-body [^{11}C]MODAG-005 PET/MR images (SUV) of a mouse over time. (**C**) Left: Average TACs for select brain areas ($n = 3$ biological replicates). Right: Average TACs illustrating in vivo biodistribution of [^{11}C]MODAG-005 in different organs. Values are shown as means ± SD. (**D**) Radio-metabolite analysis of brain and plasma samples from mice at 5 and 15 min after tracer injection ($n = 3$ biological replicates in $N = 3$ independent experiments). AU, arbitrary units; BS, brainstem; CB, cerebellum; CTX, cortex; HIP, hippocampus; M1, metabolite 1; M2*, metabolite 2*; P, parent compound; p.i., post injection; STR, striatum; THA, thalamus.

In addition, PET data were further analyzed using different approaches to define the volumes of interest and an alternative reference region. Figure S10C shows the PET analysis performed using volumes of interest based on isocontour automatic detection set to 70% to include only the region where fibril injection was performed. TACs and time-SUVR curves, as well as average SUVR, collectively illustrate higher tracer retention in the fibril-injected striata compared with the noninjected striata ($P = 0.002$). Using the left, sham-injected striatum as the reference region, elevated tracer retention was detected in the fibril-injected striata compared with the noninjected striata ($P = 0.003$) (Fig. 4D).

To determine the binding specificity of [^{11}C]MODAG-005 and to study the in vivo target engagement of anle138b in fibril-injected rats, two PET scans consisting of a baseline measurement with vehicle injection and a blocking measurement with anle138b administration were performed between 3 and 4 days after fibril injection in rats. Five minutes before tracer injection, vehicle or anle138b (1 mg/kg dose for the vehicle) was administered intravenously as a single

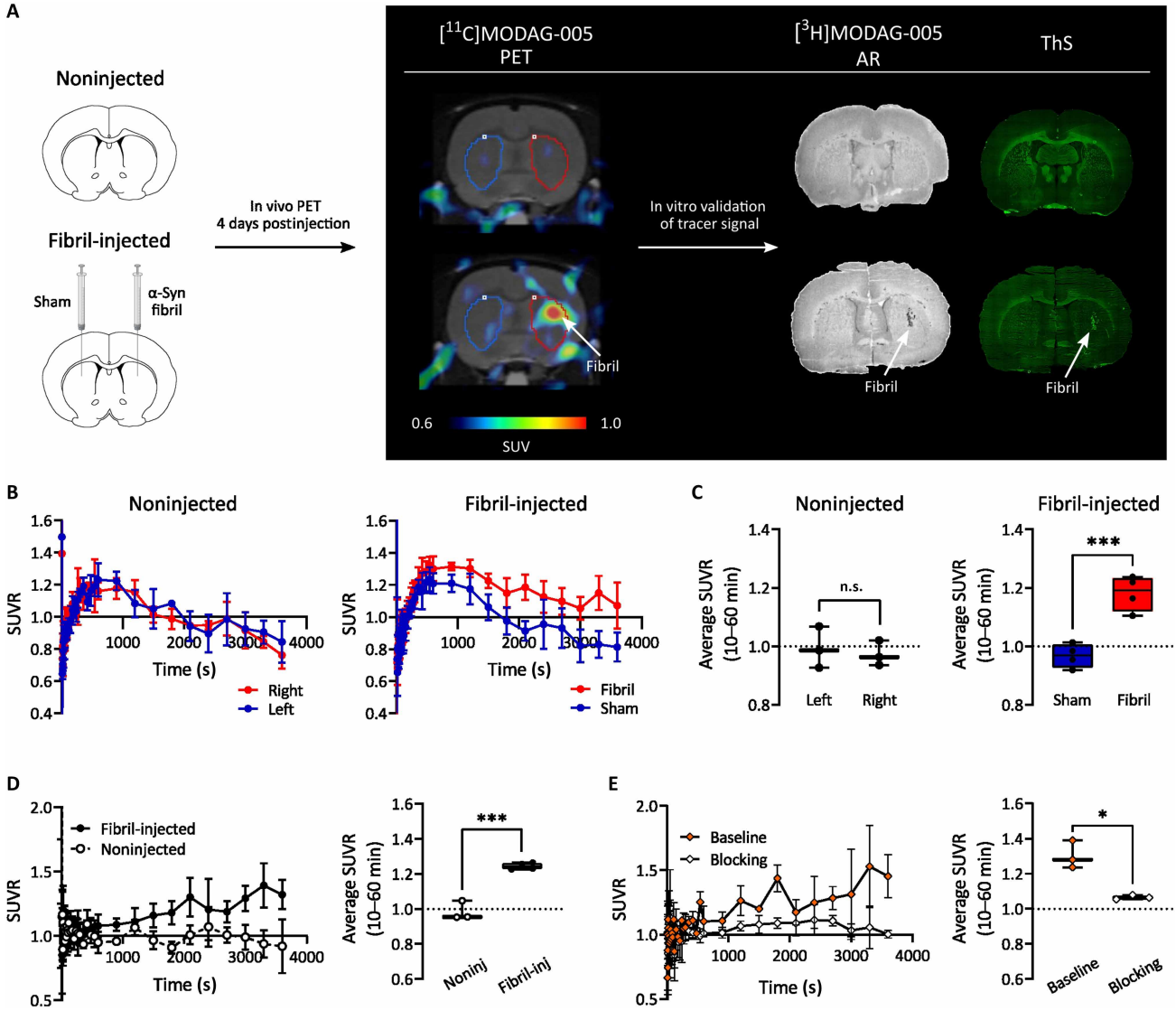

Fig. 4. In vivo characterization of [^{11}C]MODAG-005 in fibril-injected rats demonstrates specific binding to αSYN. (**A**) Representative brain [^{11}C]MODAG-005 PET images (SUV, sum of 2.5 to 60 min), [^{3}H]MODAG-005 autoradiography, and ThS validation of fibril presence in a rat. (**B** and **C**) time-SUVR curves (B) and average SUVR (C) in α-Syn fibril–injected rats ($P = 0.0003$, $n = 4$) and noninjected rats ($P = 0.54$, $n = 3$) using the cerebellum as the reference region. n.s., not significant. (**D**) Time-SUVR curves (left) and average SUVR (right) using the sham-injected, left striatum as the reference region ($P = 0.003$, $n = 3$). (**E**) Time-SUVR curves (left) and average SUVR (right) of anle138b blocking study using sham-injected striatum as the reference region ($P = 0.028$, $n = 3$). Data are the means ± SD. Unpaired two-tailed *t* tests were used for comparisons. AR, autoradiography; fibril-inj, fibril-injected; noninj, noninjected.

bolus. Administration of anle138b successfully blocked tracer binding ($P = 0.03$, sham-injected striatum as reference region) (Fig. 4E). Similar results were obtained using the cerebellum as the reference region (fig. S10, D and E): Average SUVR indicated successful blocking by anle138b, which reduced tracer binding ($P = 0.04$) in the fibril-injected striata (fig. S10E, left). In contrast, anle138b increased tracer signal in the sham-injected striata ($P = 0.02$) (fig. S10E, right).

[^{11}C]MODAG-005 showed binding in α-Syn(A30P) transgenic mouse model of PD

To study the ability of [^{11}C]MODAG-005 to detect intracellular α-Syn aggregates in vivo, we performed PET imaging in the α-Syn(A30P) transgenic mouse model of PD and age-matched wild-type mice (Fig. 5 and fig. S12). Exemplary images of [^{11}C]MODAG-005 PET and α-Syn pSer^{129} immunohistochemistry showed increased tracer signals in brain regions with high α-Syn pathology load, such as in the pons/medulla, midbrain, and hypothalamic areas in α-Syn(A30P) mice (Fig. 5A). Consistent with the α-Syn pathology distribution, elevated time-SUVR curves and average SUVR values, calculated using cortex as the reference region, reflected increased tracer retention in α-Syn(A30P) mice compared with wild-type mice in the pons/medulla (1.16 ± 0.06 versus 1.07 ± 0.07, $P = 0.004$), midbrain (0.93 ± 0.04 versus 0.88 ± 0.06, $P = 0.03$), and hypothalamus (1.28 ± 0.12 versus 1.15 ± 0.10, $P = 0.008$) (Fig. 5B). No enhanced tracer binding was detected in the amygdala ($P = 0.20$), striatum ($P = 0.08$), hippocampus ($P = 0.23$), thalamus ($P = 0.10$),

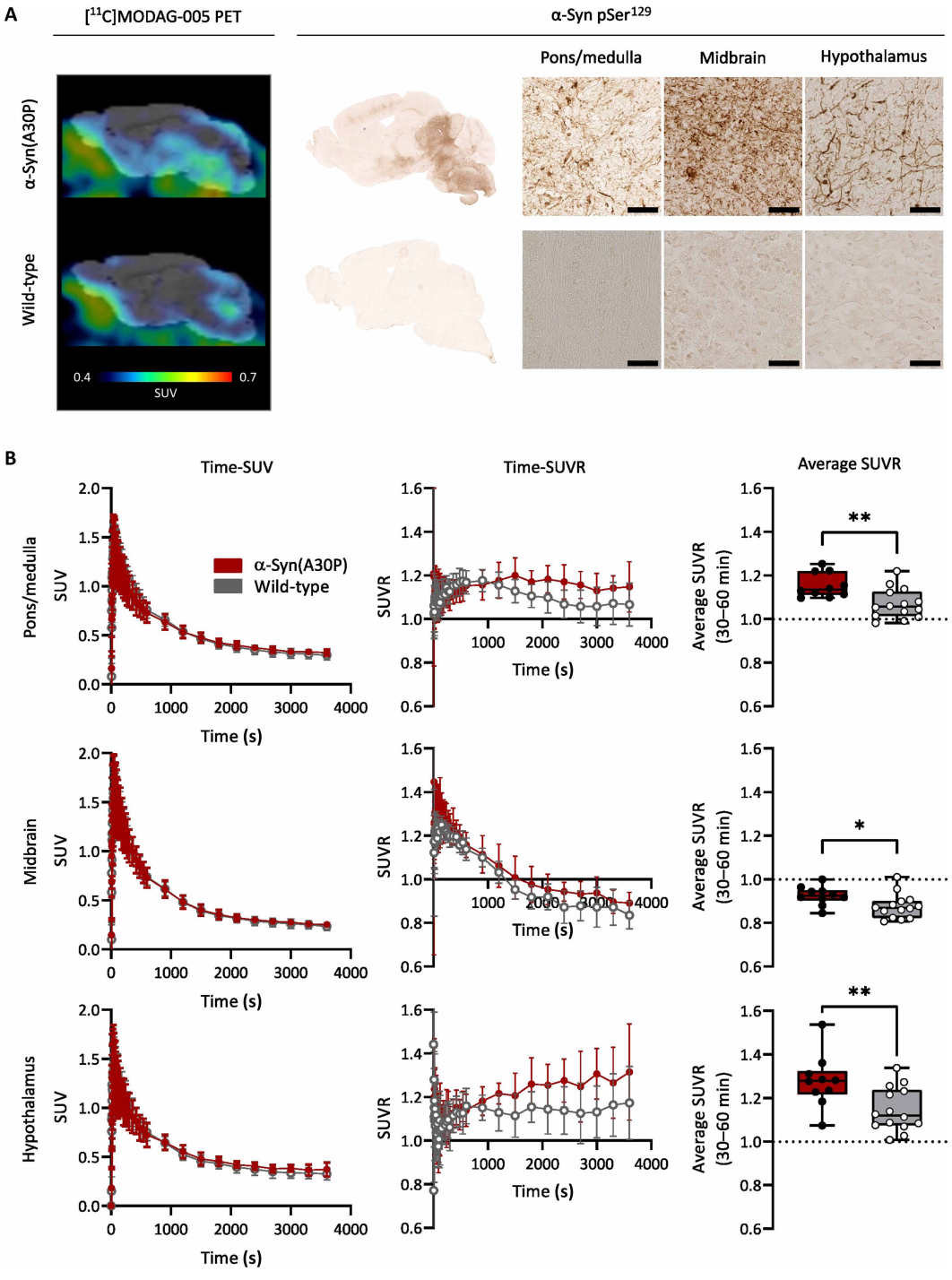

Fig. 5. [^{11}C]MODAG-005 showed elevated binding in the α-Syn(A30P) transgenic mouse model. (**A**) Representative brain [^{11}C]MODAG-005 PET images (SUV, sum of all frames) and α-Syn pSer^{129} immunohistochemistry in α-Syn(A30P) and wild-type mice. Scale bars, 50 μm. (**B**) Comparison of [^{11}C]MODAG-005 PET time-SUV and time-SUVR curves with cortex as the reference region and average SUVR in α-Syn(A30P) mice ($n = 10$, 100 ± 10 weeks old; excluding four mice with less than 1% positive α-Syn pSer^{129} staining signal; see fig. S12B) and wild-type mice ($n = 14$, 100 ± 11 weeks old) for pons/medulla (top row, $P = 0.004$), midbrain (center row, $P = 0.03$), and hypothalamus (bottom row, $P = 0.008$). $N = 1$ independent experiment. In (B), data in time-SUV and time-SUVR curves are the means ± SD. Unpaired two-tailed t test was performed to compare the average SUVR values. αSYN(A30P) mice with less than 1% positive staining signal were excluded from the main PET analysis.

and cerebellum ($P = 0.31$), where lower α-Syn pathology load was detected (fig. S12A).

Immunohistochemistry revealed high interindividual heterogeneity in the pathology load among α-Syn(A30P) mice. α-Syn(A30P) mice with less than 1% positive staining signal were excluded from the main PET analysis shown in Fig. 5 and fig. S12 (A and C). In the pons/medulla, a significant positive correlation was observed between α-Syn pSer^{129} immunohistochemistry and [^{11}C]MODAG-005 PET binding ($r = 0.47$, $P = 0.04$) (fig. S12B).

Additional SUVR analysis using the hippocampus as the reference region validated the observed differences between α-Syn(A30P) and wild-type mice, although with smaller effect sizes (fig. S12C). The suitability of the cortex as a reference region was validated by the lack of difference in the tracer retention between the two animal groups in this brain region ($P = 0.22$).

Preliminary blocking experiments in two aged transgenic and wild-type mice, performed either 900 s after tracer injection of nonlabeled MODAG-005 or anle138b or by coinjection of nonlabeled MODAG-005, demonstrated a measurable reduction in [^{11}C]MODAG-005 uptake, indicating a displaceable component of the PET signal (fig. S13, A to F). Immunohistochemistry analysis revealed no region- or genotype-specific differences in MAO-B expression in brain sections, further suggesting that elevated PET tracer binding was not due to potential off-target binding to MAO-B (score of 0 to 3, where 0 indicates no staining and 3 indicates relatively abundant staining) (fig. S14, A to C).

Characterization of [^{11}C]MODAG-005 in NHP brains indicated a favorable pharmacokinetic profile

To evaluate the tracer characteristics in wild-type nonhuman primates (NHPs) without α-Syn pathology, we performed dynamic in vivo PET imaging and plasma radio-metabolite analysis in two cynomolgus macaques (NHP 1 and NHP 2). Figure 6 (A and B) and fig. S15 (A and B) show a macaque MRI image as well as baseline and competition [^{11}C]MODAG-005 PET images of the brain summed up from 0 to 10 min and 90 to 120 min with respective TACs of selected brain regions over time. For visualization, images and TACs in units of kilobecquerels per cubic centimeter were converted to SUV in units of grams per milliliter. At baseline, rapid brain uptake with peak SUVs of 3.7 and 6.1 for NHP 1 and NHP 2, respectively, and fast washout from the brain with a clearance half-life of ~12 min (one-phase decay model from the peak) was identified (Fig. 6B and fig. S15B). After blocking with MODAG-005, we saw a similar pharmacokinetic profile, with peak SUVs of 4.7 and 4.2 for NHP 1 and NHP 2, respectively, and a clearance half-life of ~16 min. Total volume of distribution (V_T) and K_1 were estimated using a two-tissue compartment model (*18*). V_T is the activity ratio between tissue and plasma at equilibrium, and K_1 is the rate of tracer delivery from plasma to brain tissue. In the whole brain, V_T and K_1 were estimated to be 6.89 ± 1.58 ml/cm^3 and 0.49 ± 0.12 ml/cm^3 per minute, respectively. V_T values at baseline and competition were compared, revealing little differences in NHP 1 (5.11 to 6.15 ml/cm^3 versus 4.87 to 6.07 ml/cm^3) and some degree of lowered V_T in NHP 2 (7.76 to 9.81 ml/cm^3 versus 5.03 to 6.58 ml/cm^3) (Fig. 6C and fig. S15C). On the other hand, little changes between K_1 at baseline and competition were noted for both NHP 1 (0.30 to 0.45 ml/cm^3 per minute versus 0.36 to 0.63 ml/cm^3 per minute) and NHP 2 (0.49 to 0.89 ml/cm^3 per minute versus 0.51 to 0.78 ml/cm^3 per minute) (Fig. 6D and fig. S15D).

[^{11}C]MODAG-005 radio-metabolite formation in the plasma of NHP 1 and NHP 2 was determined 5, 15, 30, 45, and 60 min after tracer injection (Fig. 6E, fig. S15E, and table S3). Quantitative analysis revealed two metabolites in plasma. The amounts of parent compound were $74 \pm 1.3\%$, $29 \pm 0.3\%$, $18 \pm 1.7\%$, $14 \pm 1.0\%$, and $8.6 \pm 1.0\%$ at 5, 15, 30, 45, and 60 min after tracer injection, respectively. Heart rate (beats per min), body temperature, expired CO_2, respiration/min, pulse O_2%, % anesthetic gas, and oxygen (liters/min) throughout the scans are displayed in fig. S16.

First-in-human [^{11}C]MODAG-005 PET exhibited tracer binding in patients with synucleinopathies

After radiochemical development and preclinical evaluation, the radiochemical synthesis process for [^{11}C]MODAG-005 was transferred to a Good Manufacturing Practice (GMP) environment and further optimized to fulfill the requirements for human application, in this case following the regulations of the German Medicinal Products Act ["Arzneimittelgesetz" AMG §13(2b)]. After full disclosure, first-in-human translational PET scans with [^{11}C]MODAG-005 were performed on a highly sensitive long axial field-of-view PET scanner (Siemens Biograph Vision Quadra, Siemens Healthineers, Knoxville, USA) in four participants on the basis of individual indications, including one patient diagnosed with MSA cerebellar type (MSA-C), one patient with an overlap syndrome of MSA parkinsonian type (MSA-P) and MSA-C (MSA-C/P), and a patient with PD harboring a severe L444P mutation in the *GBA1* gene (GBA-PD), and one asymptomatic participant who wanted to rule out the presence of α-Syn aggregates in his brain. The participants gave their written informed consent both for performing the PET scan with [^{11}C]MODAG-005 and further data processing and evaluation. Clinical diagnosis for all patients was based on established clinical diagnostic criteria of the Movement Disorders Society for the diagnosis of MSA (*19*) and PD (*20*), respectively, and included evaluation of diagnostic MRI and single-photon emission computed tomography (SPECT) of the presynaptic dopamine transporter (DAT) with [^{123}I]FP-CIT {[^{123}I]N-ω-fluoropropyl-2β-carbomethoxy-3β-(4-iodophenyl)nortropane}. A [^{123}I]FP-CIT DAT scan was not available for the patient with MSA-C because the patient did not exhibit clinically overt parkinsonism at the time of diagnosis.

Figure 7 (A and B) presents axial [^{11}C]MODAG-005 PET SUVR images and, if available, DAT SPECT of patients with MSA-C, MSA-C/P, PD-GBA and the asymptomatic participant who was considered as healthy control (HC). [^{123}I]FP-CIT-SPECT images in the patient with MSA-C/P (Fig. 7A and fig. S17) showed pronounced presynaptic dopaminergic degeneration (reduced DAT availability) in the left and right striatum, with the right side displaying a markedly lower signal. [^{11}C]MODAG-005 retention showed a slightly more prominent signal on the right side, mirroring the lateralization noted in the [^{123}I]FP-CIT-SPECT images. MRI data revealed advanced cerebellar atrophy in the patient with MSA-C and the patient with MSA-C/P and pontine atrophy including indication of the "hot cross bun" sign, reflecting degeneration of pontocerebellar tracts in the patient with MSA-C/P (fig. S17A).

Overall, [^{11}C]MODAG-005 signal intensity (SUVR) was in line with the expected pattern of α-Syn deposition (fig. S18A): (i) Both patients with MSA showed intense signal in pons and cerebellar white matter (most pronounced in the patient with MSA-C), the patient with PD-GBA exhibited a less intense signal, (ii) the patient with MSA-C/P in addition exhibited a relatively strong signal in

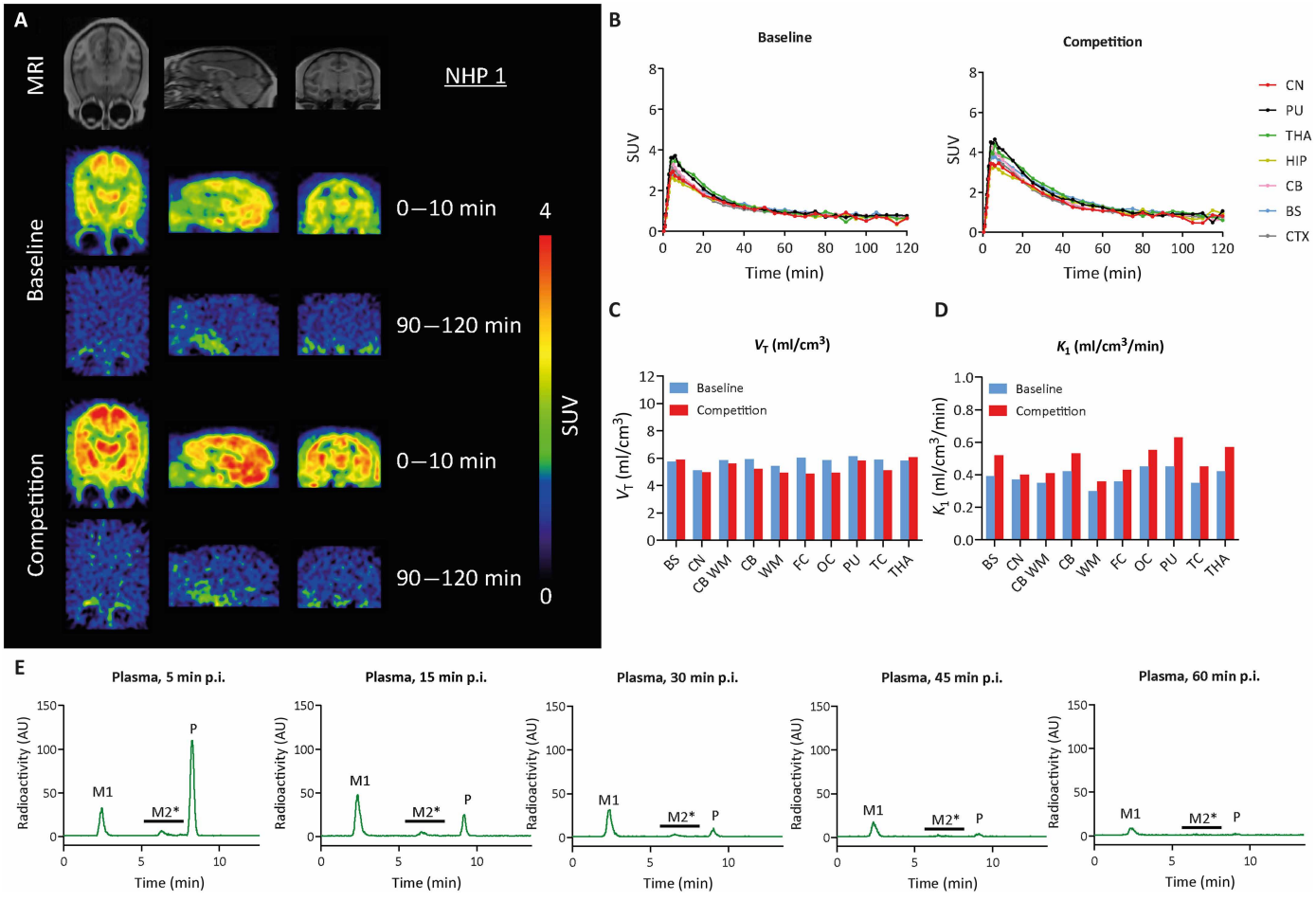

Fig. 6. In vivo characterization of [^{11}C]MODAG-005 in NHPs (NHP 1) indicated favorable tracer attributes for brain imaging. (**A**) MRI and [^{11}C]MODAG-005 PET images (SUV) at baseline and after pre-injection of unlabeled MODAG-005. (**B**) TACs of different brain regions showing high brain uptake with peak SUVs of 3.7 (baseline) and 4.7 (competition) followed by a fast clearance from the brain. (**C** and **D**) V_T (C) and K_1 (D) values estimated from a two–tissue-compartment model for the baseline and after competition with MODAG-005. (**E**) Radio-metabolite analysis of plasma samples at 5, 15, 30, 45, and 60 min after tracer injection ($n = 2$ biological replicates, no technical replicates; see fig. S12 for results from second NHP). CB WM, cerebellar white matter; CN, caudate nucleus; WM, white matter; FC, frontal cortex; OC, occipital cortex; PU, putamen; TC, temporal cortex; 2-TCM, two tissue compartment model.

both the putamen and caudate nucleus, and (iii) the patient with PD-GBA had the highest signal in the putamen and caudate nucleus and the lowest signal in the pons and cerebellar white matter. In contrast, the HC showed less tracer signal in these brain regions, in line with absence of α-Syn deposition.

To further assess the correlation of tracer binding with clinical phenotype, we calculated a score based on the ratio of SUVR in the putamen, caudate, and SN versus the pons and cerebellar white matter. The PET score was compared with the clinical score of the parkinsonian versus cerebellar phenotype calculated as described previously, showing that higher relative tracer signal in the pons and cerebellar white matter correlated with a more cerebellar clinical phenotype (fig. S18B) (*21*).

The pharmacokinetic profile in the patient with MSA-C/P and the HC is shown in fig. S19 as an example, revealing rapid uptake of [^{11}C]MODAG-005 in the brain. The occipital cortex, included in the TACs as a reference region because of its expected lack of pathology, showed a peak SUV of 2.8 and a clearance half-life of 20 min.

DISCUSSION

Here, we aimed to develop an α-Syn PET tracer, MODAG-005, on the basis of the lead structure anle138b and its derivatives, anle253b, and our previously developed PET tracer MODAG-001. We performed a detailed evaluation to characterize its binding profile from in vitro with fibrils and brain tissues to in vivo in animal models and patients with synucleinopathies.

A common challenge is the lack of detectable tracer binding to α-Syn pathology in the human brain, despite its good affinity to α-Syn fibrils (*14*, *22*). A number of recently developed α-Syn ligands showed promising in vitro binding. Yet, in vivo brain uptake and kinetics seems to require further optimization (*23*–*25*). Our previous study reported [^{11}C]MODAG-001 as a new potential α-Syn PET ligand (*14*), however, it failed to efficiently detect aggregated α-Syn from human brain tissue because of high nonspecific background binding. For other α-Syn ligands, evaluation and data analysis in animal models were not unambiguously conclusive (*6*, *26*). Several α-Syn PET tracers have recently advanced into preclinical or early

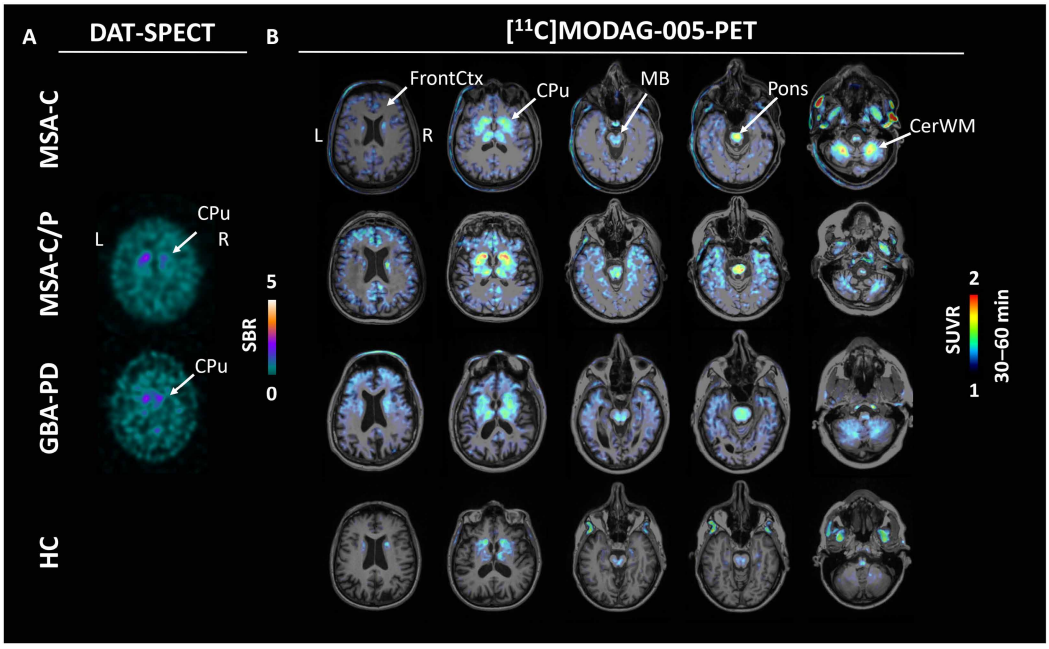

Fig. 7. [^{11}C]MODAG-005 first-in-human PET showed binding in patients with MSA-C, MSA-C/P, and PD-GBA. (**A**) DAT SPECT images showing the specific binding ratio (SBR, CPu/OccCtx-1) from a patient with MSA-C and a patient with GBA-PD, revealing presynaptic dopaminergic degeneration in the bilateral striatum (caudate and putamen), with a slightly more pronounced effect on the right side of the patient with MSA-C/P. (**B**) [^{11}C]MODAG-005 SUVR PET images (sum of 30 to 60 min) in a control participant (HC) and patients with MSA-C, MSA-C/P, and GBA-PD. Pronounced binding compared with the HC was observed in the cerebellar white matter (cerWM) and pons in the patient with MSA-C, in the bilateral caudate-putamen (CPu), midbrain and pons in the patient with MSA-C/P, and in caudate-putamen and the frontal cortex (FrontCTX) in the patient with GBA-PD. In a person without evidence of α-synucleinopathy (HC), only very faint binding was observed. L, left; MB, midbrain; R, right.

clinical evaluation, including [^{18}F]-ACI-12589 (*7*), [^{18}F]-C05-05 (*27*), and [^{18}F]SPAL-T-06 (*5*). Although developed using different assay conditions, brain tissue, and imaging paradigms, these studies share the overarching goal of establishing whether aggregated α-Syn can be visualized in vivo. Our work contributes to this rapidly evolving landscape by providing a comprehensive translational characterization of [^{11}C]MODAG-005 from in vitro binding assays to first-in-human imaging. Given the methodological variability across studies, meaningful conclusions about the relative strengths of emerging tracers will require standardized experimental frameworks and, ultimately, head-to-head evaluations in comparable models and patient cohorts.

After the identification of the demethylated MODAG-001 (MODAG-005) as a brain-penetrating metabolite, we aimed to enhance the properties by removing a major metabolite that confounds kinetic modeling. MODAG-005 additionally displays higher affinity toward human α-Syn fibrils and higher selectivity for α-Syn over tau fibrils than MODAG-001, as well as >100-fold more selective for α-Syn over $A\beta_{1\text{-}42}$ fibrils. This is in line with our recent findings revealing a high-affinity binding site in the tubular cavity of α-Syn fibrils (*28*). Potential off-target binding was tested using the Cerep diversity panel comprising 71 target proteins (receptors, transporters, channels, and enzymes) and a customized kinase panel comprising 159 different kinases. A special focus was put on MAO-B binding, because in silico analysis of different tau tracer candidates showed that they bind to the same epitope in the MAO-B enzyme as the MAO-B inhibitor selegiline. The IC_{50} value obtained in the Cerep assay provides information regarding affinity to this binding site. The determined IC_{50} of 0.8 μM is considered to be of little relevance in the context of PET imaging because the tracer concentration is below 1 nM in the brain in PET imaging studies.

The binding of [^{3}H]MODAG-005 to α-Syn pathology of human brains, particularly with an unprecedented high affinity in the MSA tissues, indicated its potential for imaging the misfolded α-Syn in human brains. Moreover, successful blocking and competition with anle138b in brain tissue from human MSA and the α-Syn(A30P) mouse model provide evidence for target engagement of anle138b given that MODAG-005 competes for the same binding site. Using [^{3}H]MODAG-005, we confirmed the binding of anle138b to aggregated α-Syn in human MSA brain tissue. Despite the presence of copathology in PD brain tissue, we detected considerable binding correlating to α-Syn immunofluorescence. A previous competition assay between MODAG-001 and SIL26 suggested that the two ligands likely target the same binding site (*14*, *29*). The latter was reported to bind to PD homogenates with a K_i value of 33.5 nM, pointing to the presence of a binding site for MODAG-001/MODAG-005 on α-Syn aggregates from the PD brain. Further validation of tracer binding in PD brain tissue will be pursued in future work.

In line with the fibril binding assay, [^{3}H]MODAG-005 autoradiography also revealed binding in PD, AD, and PSP tissues in those areas that show deposition of α-Syn, Abeta, and tau aggregates, respectively (figs. S4 to S6). Off-target binding to tau and Abeta remains a challenge for all current tracer candidates. Even when a clean off-target profile was indicated in vitro, the tracer signal may still be confounded by disease-related off-target binding in vivo. For example, [^{18}F]ACI-12589 showed binding in other neurodegenerative diseases, with increased cortical retention in individuals with AD correlated to areas of tau tracer [^{18}F]RO948 uptake despite the lack of tau binding in vitro (*7*).

We found high concordance between binding to α-Syn fibrils in vitro ($K_d = 0.20 \pm 0.03$ nM) and binding to α-Syn aggregates in

human brain tissue (K_d = 0.19 nM). A high-affinity binding site for [^{3}H]MODAG-005 remained in MSA tissue after selegiline blocking, indicating the specificity of α-Syn binding. The lack of tracer colocalization with MAO-B in MSA tissue supports the selectivity of [^{3}H]MODAG-005 at tracer concentrations used in PET imaging (below 1 nM).

On the basis of the promising in vitro binding in human tissues, MODAG-005 was labeled with carbon-11 for in vivo evaluation. Its sufficient brain uptake and rapid clearance fulfill the pharmacokinetic requirements of a central nervous system PET tracer. Because [^{11}C]MODAG-005 is the demethylated form of [^{11}C]MODAG-001, we were able to reduce the number of detectable radio-metabolites in the brain from two to one. The presence of radio-metabolite in the brain could confound kinetic modeling; therefore, analysis in human participants will be required to confirm the metabolic profile of [^{11}C]MODAG-005, given that lower species, such as rodents, have faster and more extensive metabolism compared with humans (*30*). Given the high polarity of M1 and our ability to detect the demethylated metabolite of MODAG-005 in plasma, we conclude that M1 originates from the cleaved methyl group. Consequently, this metabolite, which is present in the brain, is unlikely to have any target binding. On the basis of high-performance liquid chromatography characteristics, M2 likely represents products of phase 1 or 2 metabolism or both. However, because these metabolites do not cross the blood-brain barrier, they are not expected to interfere with PET imaging in the brain. Nevertheless, for accurate kinetic modeling, it is essential to account for the contribution of these metabolites to the total activity in plasma.

In the fibril injection rat model, [^{11}C]MODAG-005 was able to detect injected α-Syn fibrils in vivo under physiological conditions. Immunohistochemistry revealed a different pattern of GFAP and MAO-B upregulation in the brain compared with in vivo [^{11}C]MODAG-005 PET images and in vitro [^{3}H]MODAG-005 autoradiography, thereby excluding the possibility that increased tracer signal was due to MAO-B off-target binding. A successful reduction of tracer binding after anle138b blocking indicated the binding specificity of [^{11}C]MODAG-005 and provided evidence for the in vivo target engagement of anle138b. The transient SUVR fluctuations above and below 1 in normal tissue reflect kinetic differences between cerebellum and striatum rather than true biological signal, because the cerebellum shows faster wash-in and washout. Using the left striatum, whose kinetics match the injected right striatum, as the reference region kept SUVR values in control animals consistently >1, demonstrating the dependence on reference-region choice. We demonstrated that [^{11}C]MODAG-005 has improved image contrast compared with MODAG-001, showing a better SNR in the fibril-injected striatum and lower background binding in the uninjected striatum. The removal of the methyl group increases the hydrophilicity of the molecule, thereby reducing its nonspecific binding to the myelin/lipid-containing white matter brain structures (*31*).

Furthermore, [^{11}C]MODAG-005 was investigated in vivo in the α-Syn(A30P) mouse model of PD. This mouse model has intracellular Lewy body–like aggregates of the transgenic human α-Syn with the A30P mutation that causes familial PD (*32*). Compared with age-matched wild-type mice, enhanced binding of [^{11}C]MODAG-005 in α-Syn(A30P) mice was demonstrated in brain regions with strong α-Syn pathology, validated by immunohistochemistry and in line with literature reports (*32*, *33*). The observed SUV differences were modest; however, SUVR analysis indicated significant differences between transgenic and wild-type mice in regions burdened by α-Syn pathology. This was further supported by the positive correlation between α-Syn pSer^{129} immunohistochemistry and [^{11}C]MODAG-005 binding. The cortex and hippocampus were explored as reference regions for PET analysis in this animal model and showed similar results, although smaller differences were observed when hippocampus was used as the reference region. Nevertheless, the selection of the cortex over the hippocampus may be preferable because of the larger volume of the cortex and thus better statistical robustness. A limitation is the lack of a truly pathology-free reference region in the transgenic mice, which may lead to underestimation of regional group differences, particularly in the midbrain. In addition, regional differences in perfusion and tracer kinetics may influence SUVR estimates and attenuate apparent contrasts between transgenic and wild-type mice. In addition, the limited spatial resolution of 1.5-mm full width at half maximum of the Inveon PET System will lead to partial volume effects in such small brain regions, with spill-out and spill-in from adjacent tissues potentially attenuating group differences. We verified that the increase in tracer binding was not caused by MAO-B, because its expression was regardless of the pathology load. Robust blocking studies were not feasible in this mouse line because α-Syn pathology emerges only at ~2 years of age and rapidly progresses, making repeated anesthesia and longitudinal imaging impractical. Alternative models with earlier and more stable pathology will be required to further assess binding specificity.

[^{11}C]MODAG-005 showed rapid brain uptake and clearance in two NHPs. Peak SUVs were not reduced after competition with MODAG-005, pointing to low off-target binding in healthy brains. Higher baseline SUVs in the second NHP may be attributed to a higher heart rate observed during tracer injection at baseline, affecting tracer uptake (fig. S13), or low signal to noise in parent fraction measurements after 30 min for the baseline scan that may affect the arterial input function. V_T time-stability analysis (120 to 60 min) showed that V_T estimates were largely stable across regions, indicating minimal influence of late low parent fraction or metabolites. The low V_T during the NHP2 competition scan was consistent across analysis windows, supporting that the observed effect is robust to modeling duration. Given that these animals lack αSYN pathology, this effect could also reflect displacement of nonspecific or off-target interactions.

With a mean K_1 of 0.49 ± 0.12 ml/cm^3 per minute, the tracer exhibited excellent extraction from the plasma to the tissue. Competition raised K_1 values, which might be a result of blocked plasma protein binding, resulting in elevated concentrations of [^{11}C]MODAG-005 in the brain. Radio-metabolite analysis indicates a similar metabolism in rodents and NHPs.

[^{11}C]MODAG-005 was furthermore evaluated in three patients and one asymptomatic participant, who was considered an HC. Clinically, patient 1 had been diagnosed with clinically probable MSA-C and patient 2 with clinically probable MSA presenting with an overlap of MSA-P and MSA-C according to the Movement Disorders Society clinical diagnostic criteria for MSA (*19*). Patient 3 had been diagnosed with PD according to the Movement Disorders Society clinical diagnostic criteria for PD (*20*). Genetic testing of this patient revealed a severe L444P mutation in the *GBA1* gene. The absence of Alzheimer copathology was determined by analysis of cerebrospinal fluid profiles of $A\beta_{1-42}$, total-Tau, and p181-Tau concentrations, which were in the normal range in all three patients. [^{11}C]MODAG-005 demonstrated rapid brain uptake, achieving peak SUVs of 2.2 to 3.2, aligning with the aforementioned Aβ and tau

tracers (*34*, *35*). [^{11}C]MODAG-005 exhibited pronounced retention in regions anticipated to exhibit αSYN pathology, particularly in the cerebellar white matter in MSA-C and the caudate putamen, corroborating the low DAT availability observed in earlier SPECT imaging in MSA-C/P. In the thalamus, where the presence of GCIs has been previously reported (*36*, *37*), the observed enhancement of [^{11}C]MODAG-005 uptake diverges from previous studies using [^{18}F]ACI-12589 and [^{18}F]SPAL-T-06 (*5*, *7*), suggesting that [^{11}C]MODAG-005 may have a distinctive binding profile compared with the other tracers that warrants further exploration. The lateralization of tracer uptake in the patient with MSA-C/P, more pronounced on the right, mirrored the asymmetrical DAT loss observed in DAT imaging. Additionally, tracer accumulation in the pons was observed, aligning with the expected neuropathology and supporting the diagnostic accuracy of [^{11}C]MODAG-005. In the patient with GBA-PD, most pronounced differences in peak SUVR values in comparison with MSA-C and MSA-C/P were observed in the caudate, putamen, and frontal cortex, which is in line with the expected α-Syn pathology in these brain regions (*38*–*40*). Cortical tracer retention is expected, because αSYN pathology in MSA-C/P and GBA-PD may extend beyond subcortical regions to involve the neocortex, particularly in more advanced stages. Furthermore, the HC exhibited uniformly low SUVRs in regions typically affected by αSYN pathology, suggesting that the regional tracer uptake seen in patient scans reflect disease-related processes but emphasizing that larger controlled studies are required to determine diagnostic specificity. Elevated basal ganglia signal in the control may reflect high regional perfusion and tracer delivery rather than increased binding. In the absence of arterial input functions and full kinetic modeling, delivery-driven effects cannot be separated from binding-related differences.

Moreover, the correlation of the PET ratio of SUVR in the putamen, caudate, and midbrain versus pons and cerebellar white matter with the clinical score of parkinsonian versus cerebellar phenotypes (fig. S18) provides evidence that the tracer signal corresponds to the expected relative distribution of α-Syn pathology. Although SUVRs for the SN were computed and showed numerically higher correlations with αSYN pathology, reliable quantification in this small nucleus is limited by partial-volume effects at the spatial resolution of the Quadra PET/CT. We therefore used the larger midbrain volume of interest (VOI) for the main analysis, noting that higher-resolution PET systems may enable more accurate SN measurements in future studies. The exploratory correlation between regional SUVRs and clinical measures should be interpreted with caution given that it is based on only three patients with different synucleinopathy phenotypes and therefore does not permit causal inference. These preliminary observations are included for completeness but require validation in larger, disease-specific cohorts to determine whether [^{11}C]MODAG-005 uptake reflects clinically meaningful variation in αSYN pathology.

Limitations of this work are the lack of an unambiguous tracer binding to Lewy bodies and Lewy neurites in human PD tissue, as well as some lower affinity off-target binding to Aβ and tau aggregates. Because mixed protein aggregation is common in neurodegenerative diseases, any protein-specific PET tracer must be interpreted in the context of potential copathologies. αSYN aggregates frequently coexist with Aβ, tau, or other protein inclusions, as demonstrated in both human studies and NHP models (*41*). Consequently, in vivo [^{11}C]MODAG-005 uptake likely reflects the spatial distribution of αSYN aggregates superimposed on this pathological background, underscoring the importance of integrating PET findings with molecular pathology and clinical characterization to disentangle overlapping protein signatures. Another limitation regarding SUVR-based quantitative analysis of PET tracer binding is due to nondisplaceable signal and kinetic variability. SUVR-1 may approximate non-displaceable binding potential (BP_{ND}) under ideal pseudo-equilibrium conditions. However, this requires a pathology-free reference region, homogeneous nondisplaceable uptake, and stable equilibrium conditions that may not be fully met when analyzing α-Syn PET images. Regional nonspecific binding, partial-volume effects, and potential off-target saturable components may therefore contribute to SUVR variability beyond differences in α-Syn aggregate density. Larger cohorts and full kinetic modeling are needed to better establish specificity. Future blocking and occupancy studies in models or patient cohorts with α-Syn pathology will help to delineate specific from nonspecific binding and to establish the quantitative selectivity of [^{11}C]MODAG-005. Moreover, a retest study would be helpful to assess test-retest reliability of VT determination. Furthermore, the 20-min half-life of ^{11}C necessarily limits batch production and multicenter dissemination compared with ^{18}F-labeled tracers, which are more suitable for large-scale clinical deployment. Nonetheless, ^{11}C labeling offers advantages for early translational studies, including lower radiation exposure and the ability to perform multiple scans in a single day (baseline and competition paradigms). Several ^{11}C tracers, such as [^{11}C]PIB, have demonstrated substantial scientific value despite similar logistical constraints.

In conclusion, our results collectively indicated that [^{11}C]MODAG-005 is a promising tracer candidate for in vivo imaging of α-Syn pathology. Its subnanomolar binding affinity to α-Syn aggregates may provide an advantage over other tracers with lower binding. In view of the various strengths, limitations, and potentially different binding profiles of the recently investigated α-Syn tracers, [^{11}C]MODAG-005 brings its own distinctive value among the other tracers toward targeting and understanding the complexity and heterogeneity of α-Syn pathology.

MATERIALS AND METHODS

Study design

This study aimed to identify and evaluate the potential of MODAG-005 as a PET tracer for α-Syn imaging. MODAG-005 was structurally derived from the lead compounds anle138b, anle253b, and MODAG-001 (fig. S20). A detailed preclinical evaluation was performed, including both in vitro and in vivo studies, leading up to first-in-human PET imaging. Initially, a competition screening of a compound library against [^{3}H]MODAG-001 identified MODAG-005 to be a high-affinity binder to recombinant α-Syn fibrils. After tritiation, the binding affinity and selectivity of [^{3}H]MODAG-005 were determined using saturation binding assays against α-Syn, tau, and Aβ fibrils (fig. S21) and using in vitro (micro)autoradiography in animal and human brain tissues. After ^{11}C-labeling, in vivo characterization of [^{11}C]MODAG-005 was performed in healthy rodents and NHPs using PET imaging and metabolite analysis. Furthermore, in vivo binding was determined in rats intrastriatally injected with α-Syn fibrils and in the α-Syn(A30P) transgenic mouse model of PD. Last, first-in-human PET scans were performed in patients with MSA-C, MSA-C/P, or GBA-PD and an asymptomatic

participant as HC to demonstrate the translational relevance of [^{11}C] MODAG-005.

Investigators were not blinded to sample allocation, data acquisition, or analysis. Sample sizes were determined on the basis of prior studies or power calculation. Specific sample sizes and replicates for each experiment are provided in the corresponding figure legends or in Materials and Methods. No data were excluded from the analyses, other than those that were justified for the study in the α-Syn(A30P) mouse model.

The use of human brain tissues for the study was approved by the ethics committee of the Faculty of Medicine at the University of Tuebingen (ethics approval number: 813/2018BO2). All rodent experiments were conducted in compliance with the German animal protection law and with the approval of the local authorities (Regierungspräsidium Tübingen, R3/19G). Macaque experiments were conducted in compliance with all applicable sections of the Final Rules of the Animal Welfare Act regulations (Code of Federal Regulations, Title 9), the Public Health Service Policy on Humane Care and Use of Laboratory Animals from the Office of Laboratory Animal Welfare, and the Guide for the Care and Use of Laboratory Animals from the National Research Council (OLAW, current edition) (NRC, current edition). PET imaging in human participants followed the regulations of the German Medicinal Products Act ["Arzneimittelgesetz" AMG §13(2b)] with informed consent.

Statistical analysis

Statistical analysis was conducted using GraphPad Prism software. The normality of the data was assessed using the Shapiro-Wilk test. The statistical tests used for each group comparison were selected with consideration of the normality test result and are specified in the corresponding figure legends. Statistical significance was set at $P < 0.05$, with the following abbreviations used to reference P values: $*P < 0.05$; $**P < 0.01$; $***P < 0.001$; $****P < 0.0001$. Results are presented as means ± SD. All individual-level data are available in data files S1 and S2.

Supplementary Materials

The PDF file includes:
Materials and Methods
Figs. S1 to S21
Tables S1 to S3
References (*42*–*52*)

Other Supplementary Material for this manuscript includes the following:
Data files S1 and S2
MDAR Reproducibility Checklist

REFERENCES AND NOTES

1. G. Palermo, E. Del Prete, U. Bonuccelli, R. Ceravolo, Early autonomic and cognitive dysfunction in PD, DLB and MSA: Blurring the boundaries between alpha-synucleinopathies. *J. Neurol.* **267**, 3444–3456 (2020).
2. E. Gomez-Tortosa, K. Newell, M. C. Irizarry, J. L. Sanders, B. T. Hyman, α-Synuclein immunoreactivity in dementia with Lewy bodies: Morphological staging and comparison with ubiquitin immunostaining. *Acta Neuropathol.* **99**, 352–357 (2000).
3. A. C. Dupont, B. Largeau, D. Guilloteau, M. J. Santiago Ribeiro, N. Arlicot, The place of PET to assess new therapeutic effectiveness in neurodegenerative diseases. *Contrast Media Mol. Imaging* **2018**, 7043578 (2018).
4. S. Korat, N. S. R. Bidesi, F. Bonanno, A. Di Nanni, A. N. N. Hoang, K. Herfert, A. Maurer, U. M. Battisti, G. D. Bowden, D. Thonon, D. Vugts, A. D. Windhorst, M. M. Herth, Alpha-synuclein PET tracer development—An overview about current efforts. *Pharmaceuticals* **14**, 847 (2021).
5. K. Matsuoka, M. Ono, Y. Takado, K. Hirata, H. Endo, T. Ohfusa, T. Kojima, T. Yamamoto, T. Onishi, A. Orihara, K. Tagai, K. Takahata, C. Seki, H. Shinotoh, K. Kawamura, H. Shimizu, H. Shimada, A. Kakita, M. R. Zhang, T. Suhara, M. Higuchi, High-contrast imaging of α-synuclein pathologies in living patients with multiple system atrophy. *Mov. Disord.* **37**, 2159–2161 (2022).
6. J. Xiang, Y. Tao, Y. Xia, S. Luo, Q. Zhao, B. Li, X. Zhang, Y. Sun, W. Xia, M. Zhang, S. S. Kang, E. H. Ahn, X. Liu, F. Xie, Y. Guan, J. J. Yang, L. Bu, S. Wu, X. Wang, X. Cao, C. Liu, Z. Zhang, D. Li, K. Ye, Development of an α-synuclein positron emission tomography tracer for imaging synucleinopathies. *Cell* **186**, 3350–3367.e19 (2023).
7. R. Smith, F. Capotosti, M. Schain, T. Ohlsson, E. Vokali, J. Molette, T. Touilloux, V. Hliva, I. K. Dimitrakopoulos, A. Puschmann, J. Jögi, P. Svenningsson, M. Andréasson, C. Sandiego, D. S. Russell, P. Miranda-Azpiazu, C. Halldin, E. Stomrud, S. Hall, K. Bratteby, E. Tampio L'Estrade, R. Luthi-Carter, A. Pfeifer, M. Kosco-Vilbois, J. Streffer, O. Hansson, The α-synuclein PET tracer [18F] ACI-12589 distinguishes multiple system atrophy from other neurodegenerative diseases. *Nat. Commun.* **14**, 6750 (2023).
8. H. Endo, M. Ono, Y. Takado, K. Matsuoka, M. Takahashi, K. Tagai, Y. Kataoka, K. Hirata, K. Takahata, C. Seki, N. Kokubo, M. Fujinaga, W. Mori, Y. Nagai, K. Mimura, K. Kumata, T. Kikuchi, A. Shimozawa, S. K. Mishra, Y. Yamaguchi, H. Shimizu, A. Kakita, H. Takuwa, H. Shinotoh, H. Shimada, Y. Kimura, M. Ichise, T. Suhara, T. Minamimoto, N. Sahara, K. Kawamura, M. R. Zhang, M. Hasegawa, M. Higuchi, Imaging alpha-synuclein pathologies in animal models and patients with Parkinson's and related diseases. *Neuron* **112**, 2540–2557.e8 (2024).
9. C. J. Hsieh, D. Saturnino Guarino, A. J. Young, A. D. Siderowf, I. Nasrallah, A. Schmitz, C. Garcia, H. Y. Kim, E. K. Schubert, H. Lee, J. S. Perlmutter, R. H. Mach, Pilot Study of [^{11}C] HY-2-15: A mixed alpha-synuclein and tau PET radiotracer. *Cells* **14**, 1157 (2025).
10. M. B. Fares, S. Jagannath, H. A. Lashuel, Reverse engineering Lewy bodies: How far have we come and how far can we go? *Nat. Rev. Neurosci.* **22**, 111–131 (2021).
11. W. Close, M. Neumann, A. Schmidt, M. Hora, K. Annamalai, M. Schmidt, B. Reif, V. Schmidt, N. Grigorieff, M. Fändrich, Physical basis of amyloid fibril polymorphism. *Nat. Commun.* **9**, 699 (2018).
12. S. H. Shahmoradian, A. J. Lewis, C. Genoud, J. Hench, T. E. Moors, P. P. Navarro, D. Castano-Diez, G. Schweighauser, A. Graff-Meyer, K. N. Goldie, R. Sutterlin, E. Huisman, A. Ingrassia, Y. Gier, A. J. M. Rozemuller, J. Wang, A. Paepe, J. Erny, A. Staempfli, J. Hoernschemeyer, F. Grosseruschkamp, D. Niedieker, S. F. El-Mashtoly, M. Quadri, I. W. F. J. Van, V. Bonifati, K. Gerwert, B. Bohrmann, S. Frank, M. Britschgi, H. Stahlberg, W. D. J. Van de Berg, M. E. Lauer, Lewy pathology in Parkinson's disease consists of crowded organelles and lipid membranes. *Nat. Neurosci.* **22**, 1099–1109 (2019).
13. J. Wagner, S. Ryazanov, A. Leonov, J. Levin, S. Shi, F. Schmidt, C. Prix, F. Pan-Montojo, U. Bertsch, G. Mitteregger-Kretzschmar, M. Geissen, M. Eiden, F. Leidel, T. Hirschberger, A. A. Deeg, J. J. Krauth, W. Zinth, P. Tavan, J. Pilger, M. Zweckstetter, T. Frank, M. Bahr, J. H. Weishaupt, M. Uhr, H. Urlaub, U. Teichmann, M. Samwer, K. Botzel, M. Groschup, H. Kretzschmar, C. Griesinger, A. Giese, Anle138b: A novel oligomer modulator for disease-modifying therapy of neurodegenerative diseases such as prion and Parkinson's disease. *Acta Neuropathol.* **125**, 795–813 (2013).
14. L. Kuebler, S. Buss, A. Leonov, S. Ryazanov, F. Schmidt, A. Maurer, D. Weckbecker, A. M. Landau, T. P. Lillethorup, D. Bleher, R. S. Saw, B. J. Pichler, C. Griesinger, A. Giese, K. Herfert, [^{11}C]MODAG-001—Towards a PET tracer targeting α-synuclein aggregates. *Eur. J. Nucl. Med. Mol. Imaging* **48**, 1759–1772 (2021).
15. A. Maurer, A. Leonov, S. Ryazanov, K. Herfert, L. Kuebler, S. Buss, F. Schmidt, D. Weckbecker, R. Linder, D. Bender, A. Giese, B. J. Pichler, C. Griesinger, ^{11}C Radiolabeling of anle253b: A putative PET tracer for Parkinson's disease that binds to α-synuclein fibrils in vitro and crosses the blood-brain barrier. *ChemMedChem* **15**, 411–415 (2020).
16. N. R. Raval, V. Shalgunov, A. Nasser, C. A. Madsen, U. M. Battisti, M. M. Herth, L. M. Jørgensen, P. Plavén-Sigray, G. M. Knudsen, Evaluation of the α-synuclein PET radiotracer (d3)-[11C]MODAG-001 in a protein deposition pig model. *Neurosci. Appl.* **1**, 100016 (2022).
17. R. Harada, S. Furumoto, Y. Kudo, K. Yanai, V. L. Villemagne, N. Okamura, Imaging of reactive astrogliosis by positron emission tomography. *Front. Neurosci.* **16**, 807435 (2022).
18. R. B. Innis, V. J. Cunningham, J. Delforge, M. Fujita, A. Gjedde, R. N. Gunn, J. Holden, S. Houle, S. C. Huang, M. Ichise, H. Iida, H. Ito, Y. Kimura, R. A. Koeppe, G. M. Knudsen, J. Knuuti, A. A. Lammertsma, M. Laruelle, J. Logan, R. P. Maguire, M. A. Mintun, E. D. Morris, R. Parsey, J. C. Price, M. Slifstein, V. Sossi, T. Suhara, J. R. Votaw, D. F. Wong, R. E. Carson, Consensus nomenclature for in vivo imaging of reversibly binding radioligands. *J. Cereb. Blood Flow Metab.* **27**, 1533–1539 (2007).
19. G. K. Wenning, I. Stankovic, L. Vignatelli, A. Fanciulli, G. Calandra-Buonaura, K. Seppi, J. A. Palma, W. G. Meissner, F. Krismer, D. Berg, P. Cortelli, R. Freeman, G. Halliday, G. Höglinger, A. Lang, H. Ling, I. Litvan, P. Low, Y. Miki, J. Panicker, M. T. Pellecchia, N. Quinn, R. Sakakibara, M. Stamelou, E. Tolosa, S. Tsuji, T. Warner, W. Poewe, H. Kaufmann, The Movement Disorder Society criteria for the diagnosis of multiple system atrophy. *Mov. Disord.* **37**, 1131–1148 (2022).
20. R. B. Postuma, D. Berg, M. Stern, W. Poewe, C. W. Olanow, W. Oertel, J. Obeso, K. Marek, I. Litvan, A. E. Lang, G. Halliday, C. G. Goetz, T. Gasser, B. Dubois, P. Chan, B. R. Bloem,

C. H. Adler, G. Deuschl, MDS clinical diagnostic criteria for Parkinson's disease. *Mov. Disord.* **30**, 1591–1601 (2015).
21. S. Schonecker, M. Brendel, C. Palleis, L. Beyer, G. U. Hoglinger, E. Schuh, B. S. Rauchmann, J. Sauerbeck, G. Rohrer, S. Sonnenfeld, K. Furukawa, A. Ishiki, N. Okamura, P. Bartenstein, M. Dieterich, K. Botzel, A. Danek, A. Rominger, J. Levin, PET imaging of astrogliosis and tau facilitates diagnosis of parkinsonian syndromes. *Front. Aging Neurosci.* **11**, 249 (2019).
22. M. Verdurand, E. Levigoureux, W. Zeinyeh, L. Berthier, M. Mendjel-Herda, F. Cadarossanesaib, C. Bouillot, T. Iecker, R. Terreux, S. Lancelot, F. Chauveau, T. Billard, L. Zimmer, In silico, in vitro, and in vivo evaluation of new candidates for alpha-synuclein PET imaging. *Mol. Pharm.* **15**, 3153–3166 (2018).
23. T. Akasaka, H. Watanabe, S. Kaide, S. Iikuni, M. Hasegawa, M. Ono, Synthesis and evaluation of novel radioiodinated phenylbenzofuranone derivatives as α-synuclein imaging probes. *Bioorg. Med. Chem. Lett.* **64**, 128679 (2022).
24. S. Kaide, H. Watanabe, Y. Shimizu, S. Iikuni, Y. Nakamoto, M. Hasegawa, K. Itoh, M. Ono, Identification and evaluation of bisquinoline scaffold as a new candidate for alpha-synuclein-PET imaging. *ACS Chem. Neurosci.* **11**, 4254–4261 (2020).
25. S. Kaide, H. Watanabe, S. Iikuni, M. Hasegawa, K. Itoh, M. Ono, Chalcone analogue as new candidate for selective detection of alpha-synuclein pathology. *ACS Chem. Neurosci.* **13**, 16–26 (2022).
26. B. Janssen, G. Tian, Z. Lengyel-Zhand, C. J. Hsieh, M. G. Lougee, A. Riad, K. Xu, C. Hou, C. C. Weng, B. J. Lopresti, H. J. Kim, V. V. Pagar, J. J. Ferrie, B. A. Garcia, C. A. Mathis, K. Luk, E. J. Petersson, R. H. Mach, Identification of a putative α-synuclein radioligand using an in silico similarity search. *Mol. Imaging Biol.* **25**, 704–719 (2023).
27. H. Endo, M. Ono, Y. Takado, K. Matsuoka, M. Takahashi, K. Tagai, Y. Kataoka, K. Hirata, K. Takahata, C. Seki, N. Kokubo, M. Fujinaga, W. Mori, Y. Nagai, K. Mimura, K. Kumata, T. Kikuchi, A. Shimozawa, S. K. Mishra, Y. Yamaguchi, H. Shimizu, A. Kakita, H. Takuwa, H. Shinotoh, H. Shimada, Y. Kimura, M. Ichise, T. Suhara, T. Minamimoto, N. Sahara, K. Kawamura, M.-R. Zhang, M. Hasegawa, M. Higuchi, Imaging α-synuclein pathologies in animal models and patients with Parkinson's and related diseases. *Neuron* **112**, 2540–2557.e8 (2024).
28. M. Kim, D. Matthes, B. Frieg, A. Leonov, S. Ryazanov, D. Bleher, A.-K. Grotegerd, C. Dienemann, A. Giese, G. F. Schröder, S. Becker, K. Herfert, B. L. de Groot, L. B. Andreas, C. Griesinger, Structural insight into binding of novel PET tracer MODAG-005 to lipidic α-synuclein fibrils. bioRxiv 649837 [Preprint] (2025). https://doi.org/10.1101/2025.04.21.649837.
29. D. P. Bagchi, L. Yu, J. S. Perlmutter, J. Xu, R. H. Mach, Z. Tu, P. T. Kotzbauer, Binding of the radioligand SIL23 to α-synuclein fibrils in Parkinson disease brain tissue establishes feasibility and screening approaches for developing a Parkinson disease imaging agent. *PLOS ONE* **8**, e55031 (2013).
30. V. W. Pike, PET radiotracers: Crossing the blood-brain barrier and surviving metabolism. *Trends Pharmacol. Sci.* **30**, 431–440 (2009).
31. C. S. Leung, S. S. Leung, J. Tirado-Rives, W. L. Jorgensen, Methyl effects on protein-ligand binding. *J. Med. Chem.* **55**, 4489–4500 (2012).
32. M. Neumann, P. J. Kahle, B. I. Giasson, L. Ozmen, E. Borroni, W. Spooren, V. Muller, S. Odoy, H. Fujiwara, M. Hasegawa, T. Iwatsubo, J. Q. Trojanowski, H. A. Kretzschmar, C. Haass, Misfolded proteinase K-resistant hyperphosphorylated alpha-synuclein in aged transgenic mice with locomotor deterioration and in human alpha-synucleinopathies. *J. Clin. Invest.* **110**, 1429–1439 (2002).
33. H. Schell, T. Hasegawa, M. Neumann, P. J. Kahle, Nuclear and neuritic distribution of serine-129 phosphorylated α-synuclein in transgenic mice. *Neuroscience* **160**, 796–804 (2009).
34. M. Schou, K. Varnäs, J. Sandell, P. Johnström, Z. Cselenyi, S. Svensson, R. Nakao, N. Amini, L. Bergman, A. Sumic, B. Gulyas, E. Lindström-Böö, C. Halldin, L. Farde, Synthesis, radiolabeling, and in vivo pharmacokinetic evaluation of the amyloid beta radioligand [^{11}C]AZD4694 in nonhuman primates. *Mol. Imaging Biol.* **16**, 173–179 (2014).
35. L. R. Drake, J. M. Pham, T. J. Desmond, A. V. Mossine, S. J. Lee, M. R. Kilbourn, R. A. Koeppe, A. F. Brooks, P. J. H. Scott, Identification of AV-1451 as a weak, nonselective inhibitor of monoamine oxidase. *ACS Chem. Neurosci.* **10**, 3839–3846 (2019).
36. J. Brettschneider, D. J. Irwin, S. Boluda, M. D. Byrne, L. Fang, E. B. Lee, J. L. Robinson, E. Suh, V. M. Van Deerlin, J. B. Toledo, M. Grossman, H. Hurtig, R. Dengler, S. Petri, V. M.-Y. Lee, J. Q. Trojanowski, Progression of alpha-synuclein pathology in multiple system atrophy of the cerebellar type. *Neuropathol. Appl. Neurobiol.* **43**, 315–329 (2017).
37. J. Brettschneider, E. Suh, J. L. Robinson, L. Fang, E. B. Lee, D. J. Irwin, M. Grossman, V. M. Van Deerlin, V. M.-Y. Lee, J. Q. Trojanowski, Converging patterns of α-synuclein pathology in multiple system atrophy. *J. Neuropathol. Exp. Neurol.* **77**, 1005–1016 (2018).
38. S. A. Schneider, R. N. Alcalay, Neuropathology of genetic synucleinopathies with parkinsonism: Review of the literature. *Mov. Disord.* **32**, 1504–1523 (2017).
39. L. N. Clark, L. A. Kartsaklis, R. Wolf Gilbert, B. Dorado, B. M. Ross, S. Kisselev, M. Verbitsky, H. Mejia-Santana, L. J. Cote, H. Andrews, J. P. Vonsattel, S. Fahn, R. Mayeux, L. S. Honig, K. Marder, Association of glucocerebrosidase mutations with dementia with lewy bodies. *Arch. Neurol.* **66**, 578–583 (2009).
40. J. Neumann, J. Bras, E. Deas, S. S. O'Sullivan, L. Parkkinen, R. H. Lachmann, A. Li, J. Holton, R. Guerreiro, R. Paudel, B. Segarane, A. Singleton, A. Lees, J. Hardy, H. Houlden, T. Revesz, N. W. Wood, Glucocerebrosidase mutations in clinical and pathologically proven Parkinson's disease. *Brain* **132**, 1783–1794 (2009).
41. M. Bourdenx, A. Nioche, S. Dovero, M. L. Arotcarena, S. Camus, G. Porras, M. L. Thiolat, N. P. Rougier, A. Prigent, P. Aubert, S. Bohic, C. Sandt, F. Laferriere, E. Doudnikoff, N. Kruse, B. Mollenhauer, S. Novello, M. Morari, T. Leste-Lasserre, I. T. Damas, M. Goillandeau, C. Perier, C. Estrada, N. Garcia-Carrillo, A. Recasens, N. N. Vaikath, O. M. A. El-Agnaf, M. T. Herrero, P. Derkinderen, M. Vila, J. A. Obeso, B. Dehay, E. Bezard, Identification of distinct pathological signatures induced by patient-derived α-synuclein structures in nonhuman primates. *Sci. Adv.* **6**, eaaz9165 (2020).
42. M. Goedert, R. Jakes, M. G. Spillantini, M. Hasegawa, M. J. Smith, R. A. Crowther, Assembly of microtubule-associated protein tau into Alzheimer-like filaments induced by sulphated glycosaminoglycans. *Nature* **383**, 550–553 (1996).
43. J. L. Whitwell, G. U. Höglinger, A. Antonini, Y. Bordelon, A. L. Boxer, C. Colosimo, T. van Eimeren, L. I. Golbe, J. Kassubek, C. Kurz, I. Litvan, A. Pantelyat, G. Rabinovici, G. Respondek, A. Rominger, J. B. Rowe, M. Stamelou, K. A. Josephs, for the Movement Disorder Society-endorsed PSP Study Group, Radiological biomarkers for diagnosis in PSP: Where are we and where do we need to be? *Mov. Disord.* **32**, 955–971 (2017).
44. C. Philippe, D. Haeusler, M. Mitterhauser, J. Ungersboeck, H. Viernstein, R. Dudczak, W. Wadsak, Optimization of the radiosynthesis of the Alzheimer tracer 2-(4-N-[11C] methylaminophenyl)-6-hydroxybenzothiazole ([11C]PIB). *Appl. Radiat. Isot.* **69**, 1212–1217 (2011).
45. P. Larsen, J. Ulin, K. Dahlstrøm, M. Jensen, Synthesis of [11C]iodomethane by iodination of [11C]methane. *Appl. Radiat. Isot.* **48**, 153–157 (1997).
46. G. Paxinos, C. R. Watson, P. C. Emson, AChE-stained horizontal sections of the rat brain in stereotaxic coordinates. *J. Neurosci. Methods* **3**, 129–149 (1980).
47. Y. Ma, P. R. Hof, S. C. Grant, S. J. Blackband, R. Bennett, L. Slatest, M. D. McGuigan, H. Benveniste, A three-dimensional digital atlas database of the adult C57BL/6J mouse brain by magnetic resonance microscopy. *Neuroscience* **135**, 1203–1215 (2005).
48. W. K. Schiffer, M. M. Mirrione, A. Biegon, D. L. Alexoff, V. Patel, S. L. Dewey, Serial microPET measures of the metabolic reaction to a microdialysis probe implant. *J. Neurosci. Methods* **155**, 272–284 (2006).
49. M. M. Mirrione, W. K. Schiffer, J. S. Fowler, D. L. Alexoff, S. L. Dewey, S. E. Tsirka, A novel approach for imaging brain-behavior relationships in mice reveals unexpected metabolic patterns during seizures in the absence of tissue plasminogen activator. *Neuroimage* **38**, 34–42 (2007).
50. G. K. Wenning, F. Tison, K. Seppi, C. Sampaio, A. Diem, F. Yekhlef, I. Ghorayeb, F. Ory, M. Galitzky, T. Scaravilli, M. Bozi, C. Colosimo, S. Gilman, C. W. Shults, N. P. Quinn, O. Rascol, W. Poewe, Multiple System Atrophy Study Group, Development and validation of the Unified Multiple System Atrophy Rating Scale (UMSARS). *Mov. Disord.* **19**, 1391–1402 (2004).
51. C. G. Goetz, B. C. Tilley, S. R. Shaftman, G. T. Stebbins, S. Fahn, P. Martinez-Martin, W. Poewe, C. Sampaio, M. B. Stern, R. Dodel, B. Dubois, R. Holloway, J. Jankovic, J. Kulisevsky, A. E. Lang, A. Lees, S. Leurgans, P. A. LeWitt, D. Nyenhuis, C. W. Olanow, O. Rascol, A. Schrag, J. A. Teresi, J. J. van Hilten, N. LaPelle, Movement Disorder Society-sponsored revision of the Unified Parkinson's Disease Rating Scale (MDS-UPDRS): Scale presentation and clinimetric testing results. *Mov. Disord.* **23**, 2129–2170 (2008).
52. Z. S. Nasreddine, N. A. Phillips, V. Bedirian, S. Charbonneau, V. Whitehead, I. Collin, J. L. Cummings, H. Chertkow, The Montreal Cognitive Assessment, MoCA: A brief screening tool for mild cognitive impairment. *J. Am. Geriatr. Soc.* **53**, 695–699 (2005).

Acknowledgments: We thank the technical assistants M. Pethe, S. Stotz, and M. Poxleitner at the Werner Siemens Imaging Center (WSIC), University of Tuebingen for the support during experiments. We extend our appreciation to A. Ohmayer, G. Dunkel, and the Weigelin group at the WSIC for the support with the fluorescence microscope. We further thank T. Fleming Outeiro from the University Medical Center Goettingen for providing us transgenic mice for the experiment and B. Fehrenbacher for technical support with electron microscopy. **Funding:** Funding was provided by the Michael J. Fox Foundation for Parkinson's Research under grant no. MJFF16008 to K.H., A.G., and C.G.; European Union's Horizon 2020 Research and Innovative Programme under the Marie Skłodowska-Curie grant agreement no. 813528 to K.H. and A.M.; MODAG GmbH to C.G. and K.H.; Carl Zeiss Foundation to K.H.; Max Planck Society to C.G.; Deutsche Forschungsgemeinschaft (DFG; German Research Foundation) under Germany's Excellence Strategy-EXC 2067/1-390729940 to C.G.; DFG-INST 37/1145-1 FUGG to C.I.F.; Medical Faculty of the Eberhard Karls University Tübingen; and the Ministry for Science, Research and the Arts Baden-Württemberg provided funding for the long-axial field-of-view PET/CT scanner to C.I.F. **Author contributions:** R.S.S. acquired and analyzed data on autoradiography, immunostaining, fibril-injected rat model, and α-Syn(A30P) mouse model and drafted the manuscript. S.H. acquired and analyzed data on cell-free assays and pharmacokinetic and metabolic profiling in rodents and drafted the manuscript. Felix Schmidt generated and characterized recombinant α-Syn and tau fibrils and reviewed the manuscript. S.R. and A.L. designed and synthesized the ligands and precursors and reviewed the manuscript. D.B.

generated and characterized Aβ fibrils, acquired and analyzed data on microautoradiography, and reviewed the manuscript. A.-K.G. acquired and analyzed data on microautoradiography and immunostaining and reviewed the manuscript. L.K. acquired and analyzed data on pharmacokinetic and metabolic profiling in rodents and reviewed the manuscript. B.R., K.B., and T.G. evaluated clinically the patients imaged under individual medical indication, interpreted the clinical and imaging data, and reviewed the manuscript. Fabian Schmidt provided scan support and reviewed the manuscript. C.I.F. and M.R. acquired, analyzed and interpreted the SPECT and PET clinical data, and reviewed the manuscript. F.B. optimized and performed the radiochemical synthesis for preclinical experiments in rodents and reviewed the manuscript. A.M. supervised and supported the radiochemical synthesis for preclinical experiments in rodents and reviewed the manuscript. V.C.R. characterized and provided human postmortem brain tissue and reviewed the manuscript. B.D. and P.J.K. provided and genotyped α-Syn(A30P) and control mice, supported the study with immunohistochemistry, and reviewed the manuscript. C.M.S. designed, analyzed, and interpreted data on macaque experiments. K.E.H. designed and supervised the macaque experiments, interpreted the data, and drafted the macaque experiments and manuscript methods. I.P. acquired and analyzed data on (micro)autoradiography and immunostaining and reviewed the manuscript. M.S. provided electron microscopy support and reviewed the manuscript. J.L. analyzed data and reviewed the manuscript. G.R. optimized the radiochemical synthesis process for a GMP environment and optimized it for human application and reviewed the manuscript. K.H., A.G., C.G., and B.J.P. developed, conceptually designed, and supervised all experiments and drafted and reviewed the manuscript. **Competing interests:** A patent has been filed (Novel compounds for the diagnosis, treatment and prevention of diseases associated with the aggregation of alpha-synuclein, PCT/EP2020/082778) that includes MODAG-005. Inventors: A.G., Felix Schmidt, A.L., S.R., C.G., B.J.P., K.H., A.M., L.K., and S.H. A.G., Felix Schmidt, A.L., S.R., and J.L. are employed by MODAG GmbH, which retains ownership of MODAG-005, and A.G. and C.G. are shareholders of MODAG GmbH. R.S.S. is now an employee of Boehringer Ingelheim International GmbH. This work was part of her PhD thesis at Eberhard Karls University Tuebingen. C.I.F. reports consulting for Astra-Zeneca, Bayer, Novartis, Siemens Healthineers, and Telix outside the submitted work. K.B. is a consultant for F. Hoffmann-La Roche Ltd., Vanqua Bio, and the Michael J. Fox Foundation for Parkinson's Research. M.S. reports consulting for Abbvie, Bayer, Galderma, Novartis, La Roche Posay, and UCB outside the submitted work. J.L. reports speaker fees from Bayer Vital, Biogen, EISAI, Lilly, TEVA, Bial, Zambon, Esteve, Merck, and Roche; consulting fees from Axon Neuroscience, EISAI, Alnylam, and Biogen; and author fees from Thieme medical publishers and W. Kohlhammer GmbH medical publishers; and is an inventor in a patent "Oral phenylbutyrate for treatment of human 4-repeat tauopathies" (PCT/EP2024/053388) filed by LMU Munich, all activities outside the submitted work. In addition, he is an employee of MODAG GmbH and is a beneficiary of the phantom share program of MODAG GmbH. B.J.P. reports consulting for and being a shareholder of immuneAdvice GMBH, as well as consulting for MEDISO outside the submitted work. The other authors declare that they have no competing interests. **Data, code, and materials availability:** All data associated with this study are present in the paper or the Supplementary Materials. PET and MRI datasets for the data analysis will be made available at the DRYAD repository upon publication: DOI: 10.5061/dryad.f4qrfj79g. MODAG-005, MODAG-005 precursor, and α-Syn fibrils can be made available by the corresponding author (A.G.) under a material transfer agreement with MODAG GmbH. All other materials used or generated in this study are commercially available or will be supplied upon reasonable request.

Submitted 10 September 2025
Resubmitted 9 December 2025
Accepted 30 March 2026
Published 27 May 2026
10.1126/scitranslmed.aec0813

Science Translational Medicine

The PET tracer [11C]MODAG-005 targets alpha-synuclein aggregates in the brain

Ran Sing Saw, Sabrina Haas, Felix Schmidt, Sergey Ryazanov, Andrei Leonov, Daniel Bleher, Ann-Kathrin Grotegerd, Laura Kuebler, Benjamin Roeben, Fabian Schmidt, Matthias Reimold, Federica Bonanno, Viktoria C. Ruf, Bernadette Dahl, Christine M. Sandiego, Kelly E. Henry, Ioannis Papadopoulos, Martin Schaller, Philipp J. Kahle, Johannes Levin, Thomas Gasser, Kathrin Brockmann, Gerald Reischl, Christian la Fougère, Bernd J. Pichler, Andreas Maurer, Christian Griesinger, Armin Giese, and Kristina Herfert

Sci. Transl. Med. **18** (851), eaec0813. DOI: 10.1126/scitranslmed.aec0813

Editor's summary

A clinical PET tracer for alpha-synuclein (#-Syn) could transform early diagnosis of synucleinopathies such as Parkinson's disease (PD) or multiple system atrophy (MSA). Although several candidate #-Syn PET tracers are now being tested in clinical trials, the clinical development of such tracers has proven challenging. Here, Saw *et al*. describe the development of the #-Syn PET tracer [11C]MODAG-005. Structurally derived from previous tracer iterations and the #-Syn oligomer modulator anle138b, [11C]MODAG-005 exhibited high in vitro sensitivity and selectivity for #-Syn. In vivo studies in rodent models, nonhuman primates, and patients with MSA and PD demonstrated target engagement. These findings suggest that [11C]MODAG-005 is a promising #-Syn PET tracer warranting larger clinical studies further validate and characterize in vivo performance. —Daniela Neuhofer

Science Translational Medicine (ISSN 1946-6242) is published by the American Association for the Advancement of Science. 1200 New York Avenue NW, Washington, DC 20005. The title *Science Translational Medicine* is a registered trademark of AAAS.